Antibiotic-Specific Conformational Landscapes of a Multidrug Transporter

Hassan Maklad[1*], Tom Kache[2*], Aurélie Roth[1], Maria Mamkaeva[1], Cédric Govaerts[1°], Jelle Hendrix[2°] and Chloé Martens[1°]

[1]Biochemistry and Structural Biology, Université libre de Bruxelles (ULB), Boulevard du Triomphe, Building BC, B-1050 Brussels, Belgium

[2]Dynamic Bioimaging Lab, Advanced Optical Microscopy Centre and Biomedical Research Institute, Hasselt University, Agoralaan C (BIOMED), B-3590 Diepenbeek

*co-first authors

°co-corresponding authors

Abstract

Multidrug transporters are membrane proteins that can transport an ensemble of structurally dissimilar compounds and contribute to bacterial multidrug resistance (MDR) by exporting different antibiotics from the cell. However, whether they transport different substrates through a common mechanism or via distinct substrate-dependent mechanisms remains unclear. In this work, we used single-molecule Förster resonance energy transfer (smFRET) to measure time-resolved conformational dynamics of LmrP, a multidrug transporter of the Major Facilitator Superfamily (MFS). We present high-resolution conformational landscapes of LmrP in the presence of different antibiotics. Through multi-parameter Hidden Markov Modeling (mpH^{2}MM), we uncovered transient states and quantified their sub-millisecond interconversion kinetics. We observed antibiotic-dependent heterogeneity in the conformational landscape, both in accessible states and in interconversion rates. Notably, poorly or non-transported antibiotics slow down transition kinetics, pointing to rapid state interconversion as a driver of efficient transport. This suggests that MFS MDR transporters bind and export structurally dissimilar antibiotics by relying on an array of underlying conformational states with ligand-dictated interconversion rates. This work provides novel insights into the mechanism of MDR transporters and advocates for combined structure/dynamics-based drug design when targeting their function.

Introduction

Active extrusion of drugs across the cell membrane via transport proteins is a key driver of multidrug resistance in bacterial pathogens[1–3]. By decreasing the intracellular drug concentration, multidrug transporters enable bacteria to survive upon antibiotics treatment and eventually acquire genetically encoded resistance mechanisms, such as target mutation or enzymatic degradation. A molecular-level understanding of the transport mechanism of efflux pumps is a prerequisite for the development of targeted inhibition strategies to re-sensitize resistant strains [4,5].

How a single transport protein can recognize and translocate substrates with widely diverse chemical properties such as charge, size, and shape remains a fascinating enigma and, at the same time, complicates the rational design of efflux pump inhibitors. Structural adaptation to chemically diverse substrates is observed for the prototypical efflux pump AcrB, which features distinct binding pockets and multiple substrate pathways[6–8]. AcrB and its homologs, which belong to the same structural family of Resistance-Nodulation-Division (RND) transporters, play a prominent role in the emergence of multidrug-resistant phenotypes in Gram-negative bacteria [9,10]. These tripartite pumps are absent in Gram-positive bacteria, where most drug efflux systems belong to the Major Facilitator Superfamily (MFS)[1–3,11,12].

The molecular architecture of MFS efflux pumps differs markedly from that of RND pumps. MFS transporters are composed of 12 to 14 transmembrane helical segments arranged in two bundles of six helices that surround a central binding pocket [4,13,14]. MFS proteins mediate transport via the alternating access model, where the transporter alternates between inward- and outward-facing states to sequentially expose the binding site to each side of the membrane [15]. How these multidrug efflux pumps reconcile broad ligand promiscuity with a conserved MFS fold is poorly understood: do different substrates follow distinct pathways through conformational space, or do they converge onto a common sequence of structural rearrangements leading to transport? As a corollary, how multidrug transporters distinguish between transported and non-transported binders remains unclear.

59 Here, we address these questions using the multidrug transporter LmrP from *Lactococcus*
60 *lactis*[16]. LmrP is a substrate/proton antiporter from the Major Facilitator Superfamily that
61 can export several molecules including antibiotics[17,18]. We have previously investigated
62 the coupling of LmrP conformational changes to protons and ligand binding using Double
63 Electron-Electron Resonance (DEER) distance measurements on paramagnetically
64 labelled protein mutants [19–21] . These studies have shown that LmrP alternates between
65 at least two conformational states, an inward-open (IO) and an outward-open (OO) state,
66 where the protonation states of key acidic residues orchestrate the transition[19] such as
67 Asp68, a highly conserved residue in the MFS family[22,23] .In parallel, X-ray crystallography
68 characterization and DEER studies suggest that LmrP binds different ligands in an OO
69 conformation, consistent with a "one-size-fits-all" high affinity state[24]. These data were
70 obtained from solid (frozen) samples and thus conformationally fixed protein samples,
71 thereby excluding the range of dynamically interconverting structural states, including
72 short-lived ones, that compose the conformational landscape of the transporter. Recent
73 studies on transporters have revealed that heterogeneous conformational landscapes
74 composed of multiple subpopulations define transport function[25–28] . Whether this
75 underlying complexity can be leveraged to accommodate multidrug binding and,
76 subsequently, multidrug transport remains an open question.

77 Practically, an accurate depiction of a conformational landscape requires identifying
78 pathways between different conformations occupied for different time periods .To identify
79 the different states, the pathways that connect them and the underlying kinetics of the
80 transitions, we turned to single-molecule Förster resonance energy transfer (smFRET)
81 which is uniquely positioned in that regard[29–31]. In FRET, a non-radiative energy transfer
82 occurs from a donor fluorophore (D) to an acceptor fluorophore (A), where both are
83 attached to specific sites on a protein molecule [28,32]. The efficiency of the energy transfer,
84 *E*, sensitively reports on the distance between the donor and acceptor on the nanometer
85 length scale[33]. Real-time tracking of *E* for single molecules in turn allows monitoring
86 protein conformational changes and dynamics at nanometric spatial resolution combined
87 with a wide range of accessible timescales (ns-minutes).[34] Specifically, we employed
88 multi-parameter fluorescence detection with Pulsed-Interleaved Excitation
89 characterization (PIE-smFRET)[35](**Fig.1A**) to study the conformational dynamics of LmrP

90 and characterize its ligand-dependent conformational landscape. Our work reveals how
91 distinct conformational states and their interconversion kinetics together form a fine-
92 grained conformational landscape that different ligands navigate in distinct ways.

93 Results

94 Charting the conformational landscape of LmrP

95 Based on the crystal structure of LmrP in the OO conformation and the AlphaFold2 model
96 in the IO conformation[36], we selected pairs of residues with a spatial separation allowing
97 to distinguish the two states by smFRET when using ATTO 488 (donor) and Alexa Fluor
98 647 (acceptor) dyes. Specifically, one pair was selected on the extracellular side (H98
99 and M374 in TM3 and TM11 respectively) and one at the intracellular side (K9 and K404
100 in TM1 and TM12) (**Fig.1B,C**). The selected residues were replaced with cysteines into a
101 cysteine-less LmrP to enable covalent attachment of the fluorescent dyes through their
102 maleimide groups. The predicted FRET efficiency values *E*, together with the
103 corresponding expected distances between the probes in both conformations, are given
104 in (**Table S.1**). All double cysteine mutants were functionally tested by following LmrP-
105 mediated transport of Hoechst33342 in inverted membrane vesicles (**Fig. S1**). Single-
106 molecule FRET measurements were performed on the labeled LmrP molecules in
107 detergent micelles, diluted to ~50-pM concentration, and freely diffusing through the
108 femtolitre-size probe volume of the confocal microscope (**Fig.1A**). The distribution of
109 FRET efficiencies for all measured molecules was plotted as burst-wise *E* histograms.

110 At pH 7, the conformational landscape of apo-LmrP is characterized by a broad
111 distribution of *E* on the extracellular side, with a maximum around $E \approx 0.45$ (**Fig. 1D, left,**
112 **blue histogram**). On the intracellular side, the histogram displays a main central state
113 with a maximum around $E \approx 0.55$ (**Fig.1E**, **right, blue histogram**). By comparing the
114 observed to expected *E* values (**Table S.1**), we can conclude that the apo protein at pH
115 7 adopts a flexible conformational state that is predominantly closed on the intracellular
116 side, while sampling different opening magnitudes on the extracellular side.

As changes in pH modulates the conformational equilibrium of LmrP[19], we then performed smFRET measurements at pH 5, where we observe a shift in the distance distributions compared to pH 7. On the extracellular side the population centers around E ≈0.8, indicating closure upon lowering the pH (**Fig. 1D, left, orange histogram**) while, on the intracellular side, we observe the main population shifting to E≈0.3, indicating opening (**Fig. 1E, right, orange histogram).** We confirmed this observation by coupling the extracellular reporter with the D68N mutation, which is known to stabilize LmrP in the IO state [19] showing an increase of the high-FRET population at both pH 7 and 5, compared to wild-type (**Fig. S2)**. These observations are in line with our previous DEER studies[19,20] and validate the ability of smFRET to identify and distinguish different conformational states of LmrP. Importantly, smFRET analyses up to this point have reported burst-averaged values of E. However, if molecules interconvert rapidly between two (or more) FRET states while diffusing through the probe volume, these states appear as averaged histograms rather than distinct peaks, leaving conformational intermediates with potential functional significance unresolved[37,38].

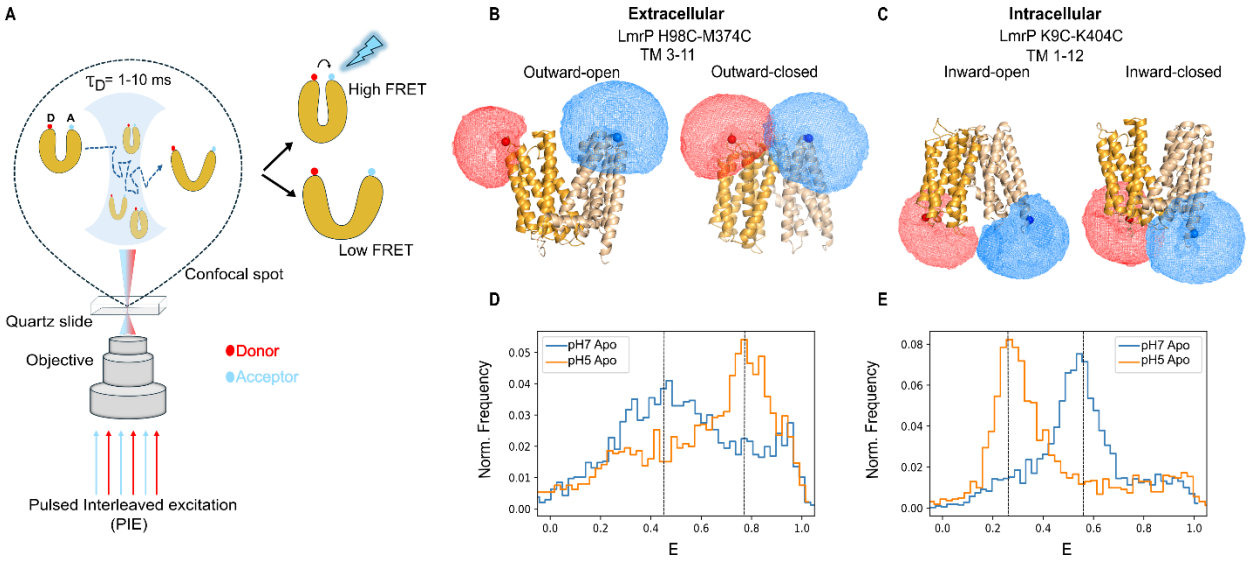

Figure 1. **smFRET charts the conformational landscape of LmrP**. **A.** Schematic illustration of the PIE smFRET experiment setup, showing the free diffusion of labelled LmrP molecules across the focal spot of an inverted fluorescence microscope. “D” and “A” correspond to donor and acceptor dyes, respectively. In the PIE setup, two spatially overlapped and alternatingly pulsing lasers are shooting at the objective to excite donor and acceptor fluorescence consecutively. Fluorescence signals of the donor and acceptor are recorded separately, and the fluorescence lifetime and anisotropy of each dye are determined.**B and C.**

Cartoon representation of LmrP helices with 98C (TM3)-374C (TM11) in outward-open **(OO)** or outward-closed **(OC)** conformations, and LmrP 9C (TM1)-404C(TM12) in inward-open **(IO)** or inward-closed **(IC)** conformations. The accessible volumes of the fluorophores ATTO488 (donor, red) and Alexa647 (acceptor, blue) are depicted as spheres. The N- and C-terminal halves of LmrP comprise TM1–6 (light orange) and TM7–12 (wheat beige), respectively. **D and E.** Burst-wise FRET efficiency histograms showing the smFRET signatures of intracellular and extracellular distance reporter mutants. The data reveals pH-dependent conformational changes of apo LmrP, with distributions recorded at **pH 7 (blue)** and **pH 5 (orange)**.

Kinetic analysis of apo LmrP reveals transient hidden states

To characterize the conformational states underlying the burst-averaged FRET histograms and the time scales at which these states interconvert, we took advantage of the advanced capabilities of the optical setup used in this work (*see Methods*). The setup records individual photons emitted by the donor and acceptor fluorophores, after their respective pulsed excitation, on the level of individual single-molecule fluorescence bursts. This enables the use of multiparameter photon-by-photon hidden Markov modeling (mpH^{2}MM) [35,39,40] to monitor FRET changes in these bursts with sub-millisecond precision [39] (**Fig. S3**). Specifically, mpH^{2}MM infers the number of conformational states a single molecule visits within a single burst, their mean *E* values, the stoichiometry *S*, the kinetic rate constants that report on how often molecules transition between given states and an estimated mean dwell time that corresponds to the average time that a molecule stays in a particular state before transitioning to another state. By integrating state identity and dwell times, we obtain a high-resolution conformational landscape for both the intracellular and extracellular reporters.

At pH 7, a three-state model was the best fit to describe the data for the distance reporters on either side of the membrane (**Fig. 2A**). When comparing the observed mean E values for each of the three states to those predicted from structural models (**Supplementary Table 1),** we observe only partial overlap. This discrepancy indicates that the protein in solution samples other states than the OO observed by crystallography or the IO predicted by Alphafold 2 modelling. We here annotated the three FRET states according to their mean *E* value: a low-FRET state **L** (*E* = 0.1–0.4), a medium-FRET state **M** (*E* = 0.4–0.7), and a high-FRET state **H** (*E* = 0.7–1.0). A subscript (E or I) is used to specify whether the measurement is on the extracellular or intracellular reporter.

170 We observe that the interconversion kinetics between the three states favor the
171 intermediate states M_E and M_I, where the protein dwells for longer (**Fig. 2A**). There is,
172 however, a noticeable difference between both sides of the protein, with a dwell time of
173 4.7 ms for the M_E and 11 ms for M_I. The dwell times for the other visited states (L_E, L_I, H_E,
174 H_I) are about equivalent (~3 ms). The mismatch in dwell times observed at the
175 extracellular versus intracellular reporters points to intrinsic flexibility of individual
176 transmembrane helices, enabling faster conformational transitions at one helix end than
177 the other.

178 This is further supported by the conformational landscape observed at pH 5. A two-state
179 model on both sides of the protein now best describes the data (**Fig.2B**), On the
180 extracellular side, it displays an interconversion between state L_E and state H_E, with mean
181 dwell times of ~3 ms and ~5 ms, respectively. On the intracellular side, the protein mainly
182 dwells for about ~15 ms in FRET state L_I and shortly transitions to the FRET state H_I for
183 ~4 ms. This differential occupancy of FRET states on each side of the transporter is
184 indicative of a protein that explores a broad structural space, extending beyond simple
185 inward–to–outward conformational transitions through rigid-body motions. Given this
186 complex and asymmetric conformational landscape, we sought a global descriptor of the
187 protein's dynamics and therefore calculated the average conformational lifetime (ACL).

188 The average conformational lifetime (ACL) is defined as the sum of dwell times divided
189 by the number of states. It provides a global measure of protein dynamics, reflecting the
190 mean time required to transition between states. For the apo protein at pH 7, the average
191 lifetime is 4.5ms, increasing to 6.9ms at pH 5. Thus, protonation of specific residues
192 simplifies the conformational landscape (from three to two states) leading to more stable,
193 longer-lived structural states. Altogether, our findings show that apo LmrP samples a
194 complex conformational landscape that is asymmetric in both state populations and
195 transition kinetics, and that this landscape is modulated by protonation.

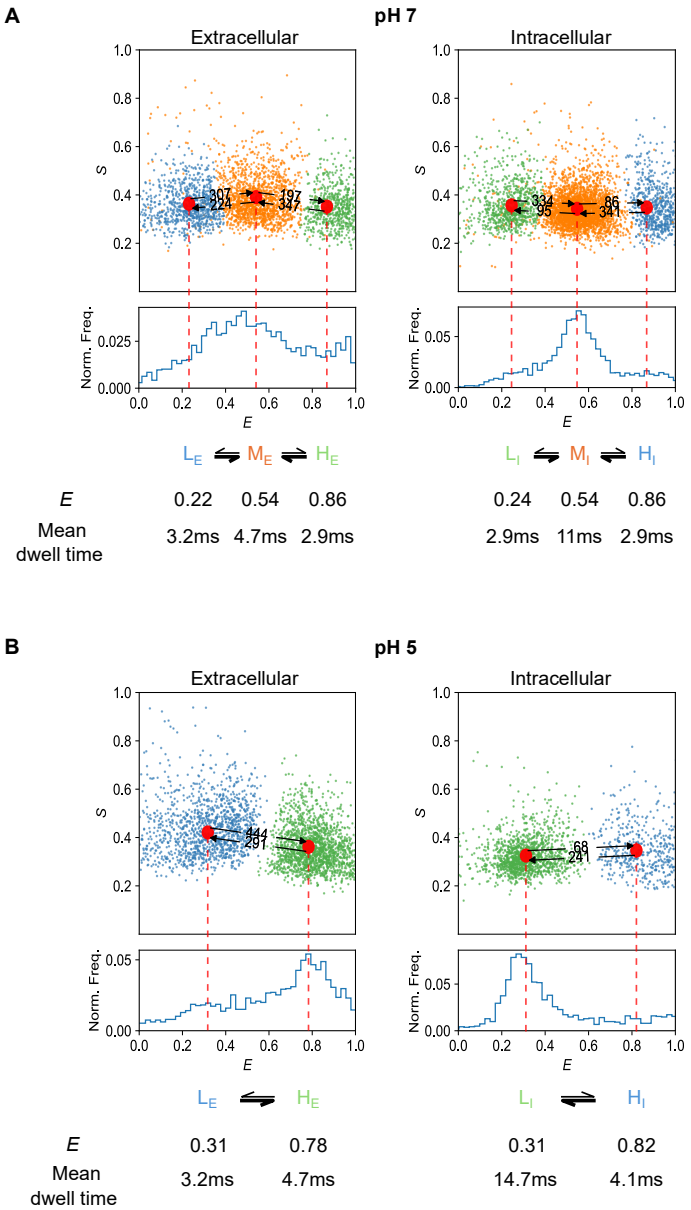

Figure 2. Kinetic analysis of apo LmrP reveals transient hidden states. A. mpH²MM analysis of LmrP in the apo state at pH 7. *Upper panel:* E–S scatter plot of individual dwells, colored according to the state assignment of the selected mpH²MM model. Red circles indicate the mean FRET efficiency (E) of each state, and the numbers above the arrows denote the transition rate constants (s^{-1}) between FRET states. *Lower panel:* Burst-wise FRET histogram showing corrected, exclusively FRET-active bursts (see Methods). The mean E value and mean dwell time (ms) for each interconverting FRET state are indicated below. Data from extracellular distance reporters are shown on the left, and intracellular distance reporter data on the right. **B**. mpH²MM analysis of LmrP at pH 5. Data are presented using the same layout and analysis as in panel **A**.

206 # LmrP displays ligand-dependent conformational dynamics

207 Next, we investigated how the conformational landscape of LmrP reorganizes in response to
208 antibiotics binding. We performed smFRET measurements in the presence of 2mM of
209 antibiotics, at pH 7, followed by mpH^{2}MM analyses. Four classes of antibiotics were tested:
210 lincosamides (clindamycin), macrolides (roxithromycin), aminoglycosides (kanamycin), and
211 β-lactams (ampicillin).

212 Quantitative kinetic state analysis using mpH^{2}MM shows that each antibiotic presents E-
213 S plots for both reporters distinct from the others, indicating ligand-dependent modulation
214 of the conformational landscape. To verify that this was not an artifact due to the presence
215 of 2 mM solute, we performed a control experiment with 2 mM glucose, which is not
216 recognized by LmrP due to its high polarity and hydrophilicity. A three-state model was
217 identified as the best fit on both sides of the membrane, with a conformational dynamics
218 and kinetic profile resembling that of the apo-state (**Fig.S4**), Thus, the changes observed
219 relative to apo are attributable to ligand binding.

220 Two aspects were considered for interpreting the impact of ligand binding: (i) how the
221 conformational landscape differs from the apo condition in terms of visited states, and (ii)
222 whether transitions between states are faster or slower on average (i.e., changes in dwell
223 times/rate constants). First, by examining changes in the conformational landscapes, we
224 observed that all ligands tested lead to a simplification of the conformational landscape
225 on one side of the transporter. Indeed, while three states were sampled on each side
226 under apo pH 7 conditions, only two states are sampled on one side and three on the
227 other for each ligand, suggesting that ligand binding reduces the number of accessible
228 states and the overall conformational heterogeneity.

229 Interestingly, the ensemble of accessible states differs as a function of the ligand.
230 Kanamycin (**Fig. 3A**), roxithromycin (**Fig. 3C**) and ampicillin (**Fig. 3D**) data fit a two-state
231 model on the extracellular side and a three-state model on the intracellular side, while
232 clindamycin binding leads to the opposite profile. Notably, these differences between
233 ligands are not reflected in their burst-averaged histograms, supporting the importance of
234 a proper kinetic analysis. For example, the conformational landscape of clindamycin as

235 revealed by the E-S scatter plot (**Fig. 3B**) differs markedly from that of the other ligands
236 and apo in terms of accessible structural states. However, its burst-averaged histogram
237 is almost identical to that of the apo, kanamycin-, and ampicillin-bound states (**Fig. 3A,**
238 **D**).

239 Analysis of kinetics of the transition between states also reveals ligand-dependent
240 modulations, with shorter dwell times for kanamycin (ACL of 3.1 ms compared to 4.6 for
241 apo), and longer dwell times (ACL of 5.8 ms) for roxithromycin. Clindamycin and ampicillin
242 show ACLs (4.0 ms and 4.6 ms, respectively) close to the apo condition. Together, these
243 data provide evidence that the conformational adaptation of this prototypical multidrug
244 efflux pump is highly diverse and ligand dependent.

245

246

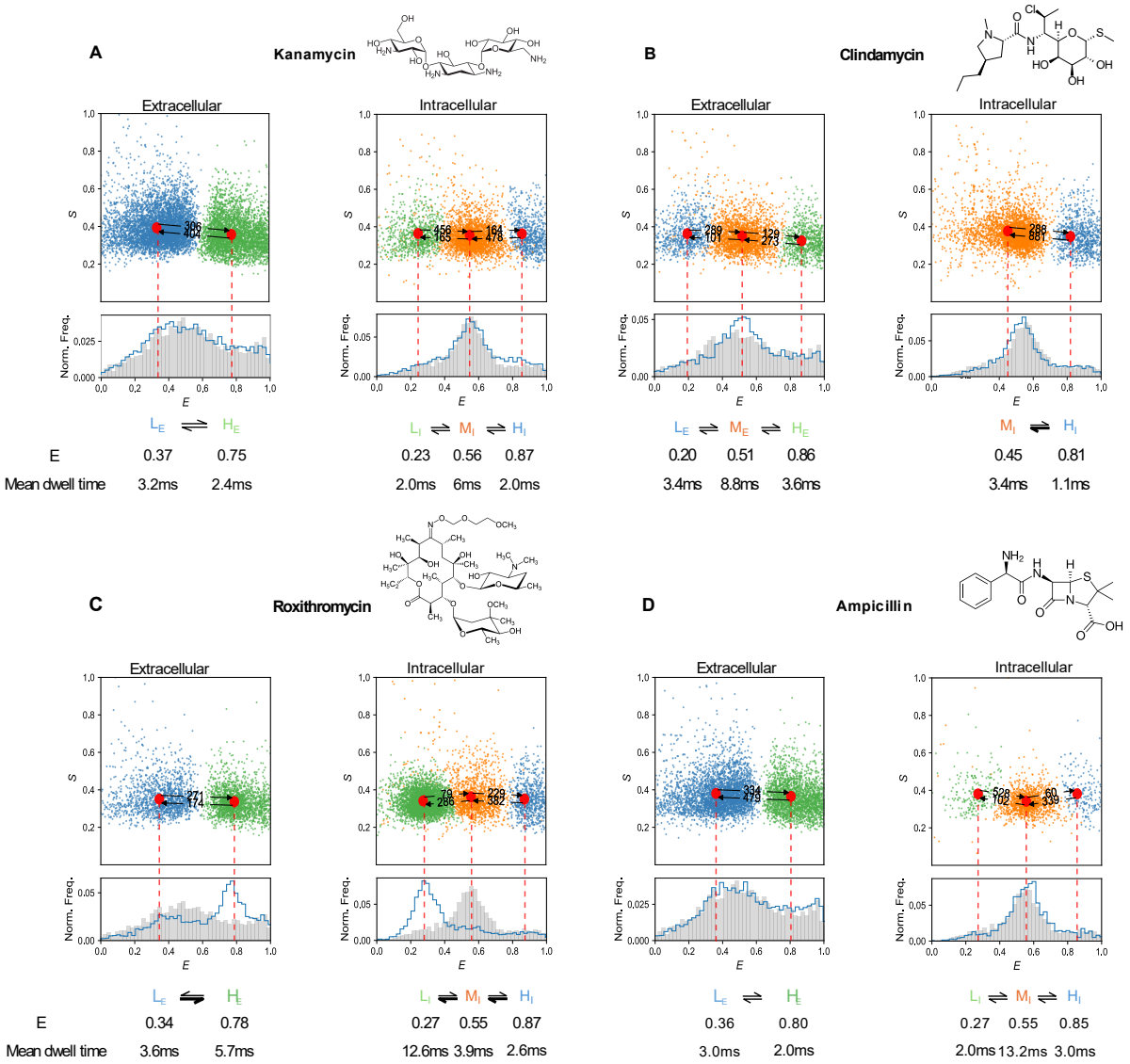

Figure 3. LmrP displays distinct ligand-dependent conformational dynamics. A-D mpH²MM analysis of LmrP in the presence of a 2 mM saturating concentration of different antibiotics. *Upper panel:* E–S scatter plots of corrected dwells, colored according to the state assignment of the selected mpH²MM model. Red circles indicate the mean FRET efficiency (E) of each state, and the numbers above the arrows denote the transition rate constants (s^{-1}) between FRET states. *Lower panel:* Burst-wise FRET histograms showing post-purified, corrected bursts. The mean E value and mean dwell time (ms) for each interconverting FRET state are indicated below. Data from the extracellular distance reporter is shown on the left, and intracellular distance reporter data on the right. The chemical structure of each antibiotic is shown adjacent to the corresponding panel (obtained from PubChem).

257 ## Different kinetic profiles have different resistance profiles

258 We speculated that the differences between ligand-induced conformational dynamics
259 could translate into a difference in transport efficiency, that would impact resistance. To
260 test this, we monitored the cell growth of *L. lactis NZ9000* strain transformed with *lmrp*-
261 containing plasmid under the control of a nisin-inducible promoter, in which the multidrug
262 transporters LmrA and LmrCD are deleted[41,42]. The assays were done for LmrP wild-type
263 (WT) and the transport-deficient mutant D68N, to compare the relative efficiency of
264 antibiotic efflux as a function of cell survival at different drug concentrations[43 44].The
265 transport-deficient D68N mutant is expressed at levels comparable to the wild type,
266 indicating that the observed differences in relative growth arise from differences in the
267 transport activity of LmrP[24] (**Fig. S5**). In the presence of kanamycin (**Fig. 4A,I**), cells
268 expressing LmrP WT required a 21-fold higher IC_{50} to inhibit growth compared to cells
269 expressing the D68N mutant. For clindamycin, we observed 12-fold increase in IC50 for
270 the WT, indicating a clear contribution of LmrP-mediated transport (**Fig. 4B,I**). In contrast,
271 The IC_{50} difference for roxithromycin was modest and did not exceed 2-folds (**Fig.4C,I**)
272 suggesting poor transport. For ampicillin, the IC_{50} ratio between WT and mutant strains
273 was close to unity, indicating that ampicillin is not transported by LmrP under the tested
274 conditions (**Fig. 4D,I**). Together, these results indicate that LmrP transports kanamycin
275 and clindamycin, while roxithromycin or ampicillin are poorly or not transported (**Fig. 4I**).

276 We next compared antibiotic-dependent cell survival with the corresponding kinetic
277 profiles of LmrP. Although the conformational landscape sampled by the isolated
278 transporter in solution is unlikely to fully mirror that in cells, this comparison allows us to
279 assess whether differences in conformational behavior are associated with functional
280 output. Therefore, we asked two main questions: (1) Does efficient transport correlate
281 with a specific structural sub-state(s)/ conformations? (2) Or is it rather the rate(s) of
282 transition between states that can be correlated with transport efficiency? To facilitate this
283 comparison, dwell times of the conformational states sampled by the extracellular and
284 intracellular reporters were plotted alongside the cell survival curves. This representation
285 allows visualization of which states are populated by the protein, and whether these states
286 are long-lived, or only transiently visited. (**Fig.4E,F,G,H**).

287 Well-transported substrates, clindamycin and kanamycin, show different conformational
288 landscapes both on the intracellular and extracellular reporters, with the state M_E visited
289 by clindamycin-bound (**Fig.4F**) but not kanamycin-bound protein (**Fig. 4E**), while the state
290 L_I is visited by kanamycin-bound (**Fig. 4E**) but not clindamycin-bound LmrP (**Fig.4F**). In
291 contrast, kanamycin-bound protein visits the same conformational landscape (**Fig. 4E**) as
292 the ampicillin-bound (**Fig. 4H**). This indicates that the conformations adopted or
293 accessible upon binding do not correlate with efficient transport. In contrast, analysis of
294 the transition kinetics between states reveals an interesting feature: the only clear
295 difference between the conformational landscapes of kanamycin (transported) and
296 ampicillin (not transported) lies in the faster transitions/ shorter dwell times (< 10 ms)
297 observed on the intracellular side for kanamycin (**Fig 4E**) compared to ampicillin (**Fig.**
298 **4H**). Transition kinetics/dwell times of clindamycin-bound LmrP are also much faster on
299 the intracellular side (**Fig. 4F**), whereas roxithromycin-bound LmrP displays long dwell
300 times (>10ms) and slow transition kinetics (**Fig.4G**). Together, these data suggest that
301 fast sampling of the conformational landscape on the intracellular side upon binding might
302 be a prerequisite for efficient transport.

303

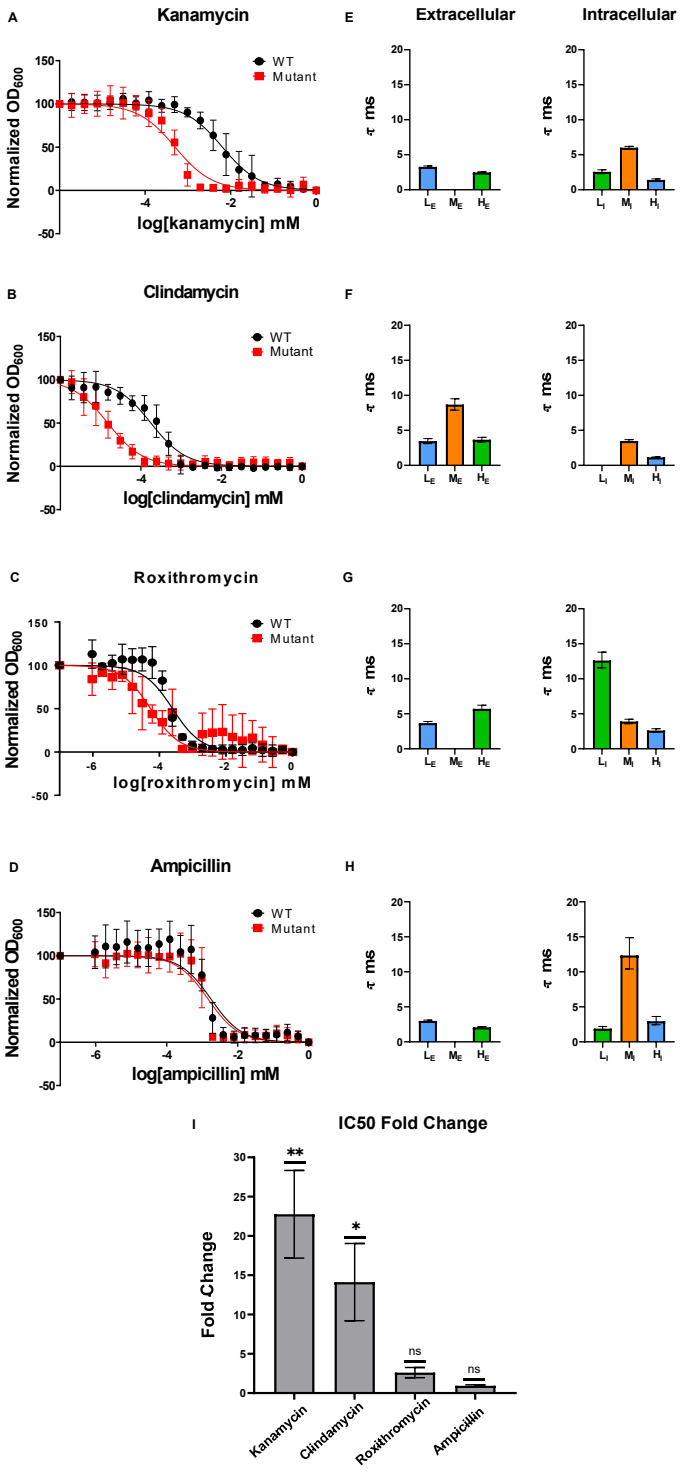

304

305 **Figure 4. LmrP-mediated antibiotic resistance. (A–D)** Growth inhibition assays of *L. lactis* expressing
306 LmrP wild-type (WT, black) or the transport-deficient mutant D68N (red) in the presence of kanamycin,
307 clindamycin, roxithromycin, and ampicillin. Non-linear regression (dose–response inhibition) was used to
308 estimate IC_{50} values. A representative assay is shown for each antibiotic; each data point represents the
309 mean ± SEM from n = 4–8 technical replicates. **(E-H)***:* Bar charts showing the mean dwell times in ms of
310 different conformational states obtained from mpH²MM analysis of smFRET data in the presence of each

antibiotic, for distance reporters located on the extracellular and intracellular sides of LmrP.**(I)** Bar chart summarizing the WT/Mutant fold change in IC50 values of the tested antibiotics, calculated from at least three independent biological experiments. The IC50 values were calculated using non-linear regression fit; log[inhibitor] vs response. Statistical significance was assessed using one sample t-test comparing fold changes in IC50 values of different biological replicas for WT and D68N mutant. P values are indicated as follows:$p \leq 0.02$(**), $p \leq 0.05$ (*), and $p > 0.05$ (ns).

Discussion

Our single-molecule FRET (smFRET) analysis shows that different antibiotics differentially reshape the conformational dynamics of the MFS multidrug transporter LmrP, giving rise to distinct ligand-dependent conformational landscapes.

LmrP and homologous multidrug transporters (e.g., MdfA, NorA, QacA) function as antiporters that exchange protons for substrates with protons entering from the extracellular medium and being released to the cytosol[45–47], while substrates are recruited either from the inner leaflet of the membrane[48] or directly from the cytosol[17]. Hence, the initial contact between the ligand and the transporter occurs on the intracellular side and involves different conformational adaptation for binding from different locations (inner leaflet or cytosol). Interestingly, clindamycin and roxithromycin are lipophilic, with logP values of 1.04 and 3, respectively (ChEMBL), while kanamycin and ampicillin are hydrophilic, with logP values of −7.6 and −2.0, respectively, suggesting different recruitment sites.

Remarkably, the conformational landscapes of LmrP in presence of kanamycin or ampicillin on the intracellular side are qualitatively similar to each other and to the apo condition (**Fig.2 and Fig.3**), transitioning between three states (L_I, M_I and H_I) with the M_I state more populated. In contrast, the conformational landscapes for the two lipophilic ligands depart markedly from the apo state; in the case of roxithromycin, the three states are present, but the L_I state is the most favored. For clindamycin, the L_i state is absent. This observation indicates that, on the intracellular side, binding of hydrophilic ligands results in minimal structural rearrangement, in contrast to lipophilic ligands, which induce significant conformational adaptation. Our work, together with that of others, points to a deviation from the canonical alternating access model of transport proposed for MFS that surmises that one conformational state is primed for binding and the other for release

342 (see Introduction). We observe that a diversity of conformations appears compatible with
343 substrate binding. Previous work on the multidrug transporter MdfA confirms this
344 observation[49]. Substrate binding of the lipophilic compound TPP^+ occurs in an occluded
345 conformation, as shown by DEER spectroscopy while substrate binding of hydrophilic
346 chloramphenicol was observed by X-ray crystallography in the inward-open
347 conformation[50].

348 However, binding does not necessarily result in transport. This work offers insight into the
349 distinction between transported and non-transported ligands in a promiscuous transporter
350 such as the MFS MDR transporter LmrP. Although the LmrP scaffold can accommodate
351 structurally diverse substrates, efficient transport appears to require the preservation of
352 structural flexibility on the intracellular side after binding. We correlated the kinetic profiles
353 obtained for the isolated protein with resistance assays in bacteria and observed that
354 higher transport efficiency was associated with a flattening of the conformational
355 landscape charted by the intracellular reporter. Specifically, clindamycin and kanamycin,
356 are both efficiently transported and induce accelerated transitions between states relative
357 to the apo-state at pH 7 (**Fig. 5A, B**). This is indicated by the short mean dwell times
358 below 6 ms for clindamycin and kanamycin (**Fig. 3A, B**), respectively, compared to up to
359 11 ms for the apo-state (**Fig. 2A**). On the other hand, ampicillin traps LmrP in the M_I state
360 for 13.2 ms (**Fig. 3D**), while roxithromycin traps it in state L_I state for 12.6ms **(Fig. 3C).**
361 Within the framework of this hypothesis, it is not the specific state that determines efficient
362 transport, but rather the height of the kinetic barrier between states. (**Fig 5**)**.** Further
363 studies with additional ligands, whether transported or not, are required to confirm this
364 hypothesis.

365 This study opens new avenues for developing strategies for functional control of multidrug
366 resistance pumps. Our results reinforce the notion that designing ligands to target a
367 specific conformational state (e.g., inward- or outward-facing) is unlikely to be a viable
368 approach, as multidrug transporters can operate effectively across a broad
369 conformational landscape. Instead, interfering with the dynamics of state interconversion
370 i.e., kinetically trapping the transporter in whichever conformation it happens to encounter
371 the ligand appears more promising, as stopping conformational cycling is sufficient to

372 block transport activity. In practical terms, such kinetic trapping could be achieved by
373 designing binders that primarily increase the activation barriers between conformational
374 states locking moving domains, stabilizing inter-domain interfaces, thereby slowing or
375 arresting the conformational cycle irrespective of the exact structural state that is
376 populated. In this context, a promising proof-of-principle approach was recently
377 demonstrated for the multidrug transporter NorA, where a Fab locked the transporter in a
378 single conformation[43], here the outward-open. Peptide derivatives designed from the
379 CDR3 recognition region of this Fab efficiently inhibited NorA-mediated efflux of various
380 drugs, including ciprofloxacin. Together, these findings, consistent with the current
381 understanding of the remarkable plasticity of such transporters, pave the way for novel
382 drug design strategies that move beyond a static structural view and incorporate the role
383 of dynamic structural rearrangements.

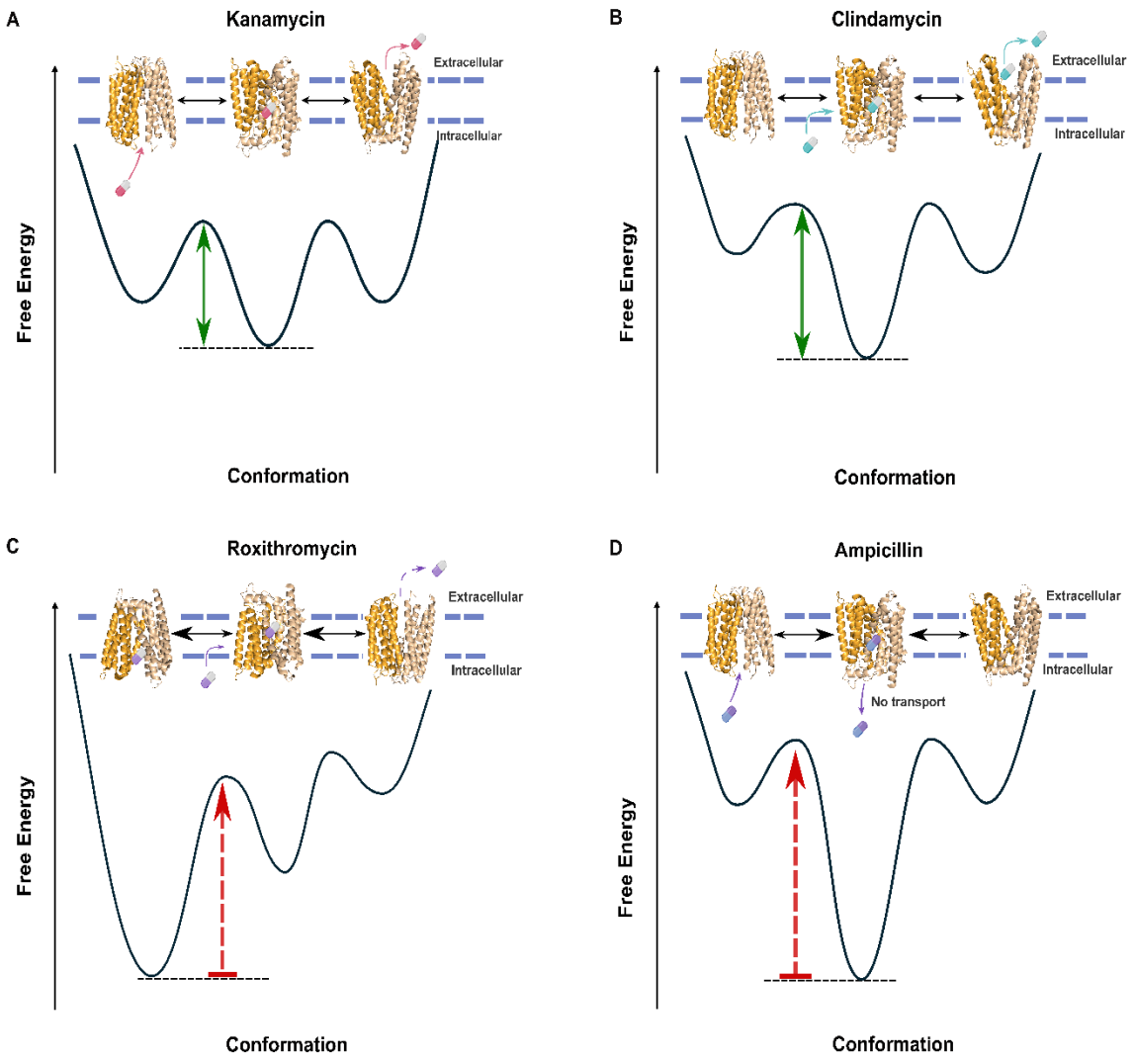

Figure 5. The conformational model of LmrP. **A-D** Schematic free-energy landscapes corresponding to the conformational cycle of LmrP with the antibiotics: kanamycin, clindamycin, roxithromycin, and ampicillin. The drug-bound profiles highlight distinct energetic preferences for conformational states which either lead to transport (low kinetic barrier indicated by a green arrow) or to inhibition (red kinetic barrier indicated by a red arrow). Horizontal dashed lines indicate the energy level of the most stable state in each condition. In-set is the cartoon illustration of the conformational landscapes of LmrP with each antibiotic. Cartoon illustration of LmrP conformations are based on outward-open LmrP structure (PDB:6T1Z), inward-open (published AlphaFold2 model), outward-occluded and extra-outward-open (Chai discovery model followed by manual fine-tuning, see *Methods*).

Materials and Methods

Bacterial strains, plasmids and growth conditions

397 LmrP was expressed in the *L. lactis* NZ9000 strain that is deleted of the known ABC
398 multidrug transporters LmrA and LmrCD[41,42]. We used the in-home pHLP5-3C plasmid, a
399 derivative of the *L. lactis* expression vector pNZ8048 carrying the lmrP gene coding for
400 the C-terminally 6 Histidine-tagged LmrP[51]. Briefly, cells were grown at 30 °C in M17 broth
401 supplemented with 0.5% (w/v) glucose and 5 µg/mL chloramphenicol until the OD660
402 reaches 0.7. The overexpression of LmrP was then induced by the addition of 1:1000
403 dilution of the supernatant of the nisin-producing *L. lactis* strain NZ9700[52,53]. After 2h of
404 induction at 30 °C, cells were harvested by centrifugation at 7000 ×g.

405 **Design and construction of the mutants**

406 For each distance reporter, two residues were selected to be mutated into cysteines
407 based on the structure of LmrP obtained by X-ray crystallography in the outward-open
408 conformation (PDB:6T1Z) as well as on the AlphaFold predicted model of the inward-
409 open conformation[36]. Cysteines were placed at the extracellular and intracellular
410 extremities of chosen TMs while avoiding mutating conserved residues. The expected
411 FRET efficiencies were estimated by simulating the fluorescent probes' accessible
412 volume[54] so that they are separated by a distance within the Förster radius, 56.8 Å in this
413 case [55]. The accessible volume (AV) clouds were simulated using the parameters given
414 for ATTO488 and Alexa647 in [55].

415 The plasmid template was first methylated using the dam methyltransferase (NEB),
416 following the manufacturer's recommendations and as described in[56] Mutations were
417 introduced by site-directed mutagenesis using the Pfu DNA polymerase (Promega) in the
418 in-home pHLP5 plasmid, in which an alanine had previously replaced the only
419 endogenous Cys270[20]. The primers were designed as described in[57]. After
420 transformation, plasmid DNA was extracted and verified by sequencing.

421

422 **Preparation of inside-out membrane vesicles**

423 As previously described[51] ,cells were washed in 50 mM HEPES pH 7. They were
424 resuspended (10 mL for each L of culture) in the same buffer supplemented with 7 mg/mL

425 of lysozyme from chicken egg whites (BioChemica), 10µg/mL Deoxyribonuclease I from
426 bovine pancreas DNAse I (VWR), 10 mM MgSO4, and 50mM Dithiothreitol (DTT). After
427 90min incubation at 30 °C, cells were homogenized with a Potter-Elvehjem-type tissue
428 grinder and lysed by four passes at 1000–1500 bars using a high-pressure homogenizer.
429 Cell debris and undisrupted cells were subsequently eliminated by centrifugation at
430 17,000 × g. Inside-out membrane vesicles were then isolated by ultracentrifugation of the
431 supernatant at 100,000 ×g for 2h at 4°C. Membranes were resuspended in a pH7 buffer
432 of 100 mM HEPES, 300 mM NaCl, 20% (w/v) glycerol (5 mL buffer/L culture) and 1mM
433 DTT.

434 **Transport assays**

435 The transport activity of LmrP mutants was assessed by measuring Hoechst fluorescence
436 (EX 355 nm, EM 457 nm) decay over time at 30°C, based on previously published
437 protocols[41,51] .Briefly, inside-out membrane vesicles of LmrP-expressing cells (~1mg
438 proteins) were diluted in transport buffer (50 mM HEPES, 2mM MgCl2, 300 mM KCl, pH
439 7.4) with 0.3µM of Hoechst (Invitrogen). The addition of 3 mM of ATP-Na2 in 50 mM
440 HEPES pH 6.8 buffer supplemented with 250 mM MgSO4 allows the generation of a
441 proton gradient by activating the endogenous F0F1-ATPase. Active extrusion of Hoechst
442 by LmrP is detected by a decrease of fluorescence. Addition of 1µM of the ionophore
443 nigericin dismisses the proton gradient and Hoechst is no longer actively extruded by
444 LmrP, causing the fluorescence to increase. Raw data were normalized for fluorescence
445 intensities relative to the initial fluorescence prior to ATP addition.

446 **LmrP purification and labelling for smFRET**

447 Inside-out membrane vesicles were solubilized in a solution of 2.5% (w/V) n-dodecyl- β –
448 D-maltoside (β-DDM) in water with 1 mM DTT. After 1.5 h incubation on a rotating wheel
449 at 4 °C, the insoluble part was removed by ultracentrifugation at 100 000 × g for 1 h. The
450 supernatant was batch-incubated with Ni^{2+}-nitrilotriacetate affinity resin (Ni-NTA; Qiagen;
451 500 µL resin/L of culture) with 10mM imidazole at 4°C for 2h. The resin was pre-
452 equilibrated with buffer A (50mM HEPES, 150mM NaCl, 10% (w/V) glycerol, 20mM
453 imidazole, and 0.05% (w/V) β-DDM, pH 7). After the incubation, the slurry was transferred

454 into a polypropylene column, the flow-through discarded, and the resin was washed with
455 8 CV of buffer A, supplemented with 0,5mM DTT. LmrP was then eluted by stepwise
456 additions of buffer B (buffer A with 250mM imidazole and 0,5mM DTT). The more
457 concentrated fractions were pooled together. Imidazole and DTT were removed just prior
458 to labelling using a desalting column (Disposable PD10 desalting columns, GE
459 Healthcare) previously equilibrated with labelling buffer (50mM HEPES, 150mM NaCl and
460 0.02% (w/V) β-DDM, pH 7.5) that was degassed in vacuum/N2 under continuous stirring.
461 LmrP was concentrated to approximately 100μM using a 50kDa MWCO concentrator
462 (Amicon, GE Healthcare) and then labelled with the donor ATTO488 (ATTO 488
463 maleimide, ATTO-TEC GmbH) and the acceptor Alexa647 (Alexa Fluor 647 maleimide,
464 Life Technologies Europe BV). 250μM Alexa647 and 100μM ATTO488 were mixed in the
465 degassed Labelling buffer and 50μM of LmrP was added for 2h at RT. Unreacted dye
466 was removed on a desalting column, and the labelled protein was run on an SDX-200
467 10/300 GL (GE Healthcare) size exclusion chromatography column in SEC buffer (50 mM
468 HEPES, pH 7, 150 mM NaCl, 10% (w/v) glycerol, and 0.02% (w/v) β-DDM). The efficiency
469 of the labelling was checked via UV-visible absorbance at 280nm, 501nm, and 650nm to
470 estimate the amount of LmrP, ATTO488, and Alexa647, respectively, after correcting the
471 280nm peak for the dyes' absorbance.

472 **Confocal Multiparameter-PIE Microscope setup**

473 The experimental measurements were recorded using a home-built multiparameter
474 fluorescence confocal microscope operating with pulsed-interleaved excitation [34,35,58].

475 Two pulsed lasers were used for excitation with excitation wavelengths of 483nm (LDH-
476 P-C-470, Picoquant, Berlin, Germany) and 635nm (LDH-P-C-635B, Picoquant, Berlin,
477 Germany) with clean-up filters for both excitation sources (Chroma ET485/20x, F49-
478 482,AHF Analysentechnik, Tübingen, Germany and Chroma z635/10x, Picoquant, Berlin,
479 Germany). Both lasers were operated with a pulse frequency of 26.67 MHz (PDL 828
480 "Sepia 2", Picoquant, Berlin, Germany) (and delayed by 18ns relative to each other. The
481 laser beams were reflected using mirrors and dichroic mirrors into an optical fiber (60FC-
482 4-RGBV11-47 and PMC-400Si-2.6-NA012-3-APC-150-P, Schäfter und Kirchhof,
483 Hamburg, Germany). After the fiber, the beams were collimated (60FC-L-4-RGBV11-4 7,

484 Schäfter und Kirchhoff, Hamburg, Germany), passed through a linear polarizer (Codixx
485 VIS-600-BC-W01, F22-601, AHF, Tübingen, Germany) and reflected into the backport of
486 a microscope body (X70, Olympus Belgium NV, Berchem, Belgium) using a 3mm thick
487 excitation polychoric (zt 405/488/561/640tpc, AHF, Tübingen, Germany) and two mirrors.
488 The power of the excitation sources was measured and adjusted to the desired power
489 before the beam entered the microscopy body using a laser power meter. Excitation
490 powers of 100µW and 50µW were set for the 483nm and 635nm excitation sources,
491 respectively. The excitation lasers were focused into the sample volume using a water-
492 immersion objective lens (UPLSAPO-60XW, Olympus), and the confocal spot was
493 focused about 10µm into the measured solution. The emission was collected through the
494 objective lens, transmitted through the polychroic mirror, focused through (AC254-200-A-
495 ML, Thorlabs, Bergkirchen, Germany) a 75 µm-pinhole (P75S, Thorlabs), and collimated
496 again (AC254-50-A-ML, Thorlabs). Subsequently, the emission was spectrally separated
497 using dichroic mirrors. The 483-nm emission (referred to as B) is reflected (Chroma
498 T560lpxr, F48-559, AHF), filtered (Chroma ET525/50m, F47-525, AHF). The 635-nm
499 emission (R) was passed through and filtered (Chroma ET705/100m, AHF). Both
500 emission beams are furthermore separated according to their polarization (BS252,
501 Thorlabs) and then detected using four avalanche photodiodes, two for the parallel (∥)
502 and perpendicular (⊥) polarization components of each spectral range (PD-100-CTE,
503 MPD for B∥ and B⊥; EG&G SPCM-AQR12/14 for R∥ and R⊥). The detector outputs were
504 routed (HRT-82, Becker & Hickl, Berlin, Germany) to and recorded with a TCSPC card
505 (SPC-630, Becker & Hickl). The experimental TCSPC data were recorded in a 12-bit
506 format encoding for the total experiment time ("macrotime"), time relative to the laser
507 excitation pulse ("nanotime"), and a detector identification signal. Data processing of the
508 recorded TCSPC data is discussed in the section Burstwise Data Processing([35,59]).

509 **Single-Molecule FRET Data Recording**

510 Before performing sample measurements, the alignment of the smFRET microscope was
511 confirmed by measuring a mixture of 5 nM each of ATTO488-COOH and ATTO655-
512 COOH in water. The setup was aligned to achieve brightnesses of > 100kHz for the donor
513 and >70kHz for the acceptor detectors with laser excitation powers of 100 and 50 µW for

514 the donor and acceptor excitation laser, respectively. The purified and double-labeled
515 LmrP protein was diluted in measurement buffer: 50 mM HEPES pH 7 (adjusted for 20°C,
516 Sigma-Aldrich), 150 mM NaCl (VWR Normapur), 0.02 % β-DDM (w/V, Carl Roth) to a
517 concentration of approximately 50 pM and to achieve a burst event frequency of 10 to 20
518 / s. For measurements in the presence of a substrate, the burst concentration-diluted
519 solution of protein was allowed to incubate with the indicated substrate concentration on
520 ice for 30 minutes. The measurement buffer was recorded without the protein to confirm
521 the absence of an excessive and potentially interfering signal contribution. This was
522 repeated for each substrate with the same concentration as in measurements with labeled
523 protein. The sample solution was recorded on an 8-well Nunc Lab-Tek chambered 1.0
524 cover glass (Thermo Fisher Scientific). The confocal observation volume was focused
525 about 10 µm above the surface of the cover glass into the sample solution. Measurements
526 were recorded at room temperature (approximately 22 °C).

527 **Burst-wise Data Processing**

528 The experimentally recorded TCSPC data were processed by converting the recordings
529 to the HDF5 format using the phconvert Python module (phconvert 2024). The data were
530 further processed using the FRETbursts module[60]. The detector identification signals and
531 detector timing ranges, which indicate the spectral range and polarization (the photon
532 records of the two polarization channels per spectral channels were summed) of the
533 detected photon, were assigned to either the donor excitation/donor emission ($D_{ex}D_{em}$),
534 donor excitation/acceptor emission ($D_{ex}A_{em}$), or acceptor excitation/acceptor emission
535 ($A_{ex}A_{em}$) to disentangle the recorded signal according to the pulsed-interleaved excitation
536 scheme. The background contribution was estimated using a single-exponential fit with a
537 30-second time window and a background threshold of less than 1.7. Individual burst
538 events were identified using an all-photon burst search with a 20-photon sliding window
539 and a minimum burst event acceptance threshold of 7-times the background count rate.
540 Burst-wise parameters, such as the burst-wise FRET efficiency *(E)* or stoichiometry *(S),*
541 were automatically calculated by the FRETbursts module (see section Calculation of
542 Burstwise Parameters and Parameter Correction)[60]. To remove bursts that only contained
543 signal from either the donor or acceptor dye, a minimum of 60 $D_{ex}D_{em}$ or $D_{ex}A_{em}$ photons

544 and at least 40 $A_{ex}A_{em}$ photons were required. The distribution of bursts in *E* and *S* was
545 assessed for the presence of a FRET-active population with *S* of around 0.5 which
546 indicates emissions from both the donor and acceptor dyes. This removes bursts with
547 predominantly non-emissive donor or acceptor dyes (with *S* of 1 and 0, respectively). The
548 photon-count filtered set of bursts was loaded into the burst mpH^{2}MM module for removal
549 of short-lives donor or acceptor blinking states using a four-state mpH^{2}MM fit [61]. All photon
550 streams ($D_{ex}D_{em}$, $D_{ex}A_{em}$, and $A_{ex}A_{em}$) were used for mpH^{2}MM fitting. The fit results were
551 used to filter out individual burst events in which a molecule ever visited a non-FRET-
552 active state during the transition time through the observation volume. This was achieved
553 by identifying the states with near-1 and near-0 *S* and removing such burst events from
554 the list of bursts. This procedure removed about half of the burst events from the
555 presented data. A second round of mpH^{2}MM analysis was performed with the cleaned
556 dataset to describe the dynamics of the data (see supplementary data for a step-by step
557 overview of the data processing and Hidden-Markov Model Fitting)[39,60].

558 **Calculation of Burst-wise Parameters and Parameter Correction**

559 Using the pulsed interleaved excitation (PIE) scheme for smFRET, the FRET efficiency
560 is defined as

561
$$E = \frac{I_{DA} - \alpha\, I_{AA} - \delta\, I_{DD}}{I_{DA} - \alpha\, I_{AA} - \delta\, I_{DD} + \gamma I_{DD}}$$

562 and the stoichiometry as

563

564
$$S = \frac{I_{DA} - \alpha\, I_{AA} - \delta\, I_{DD} + \gamma I_{DD}}{I_{DA} - \alpha\, I_{AA} - \delta\, I_{DD} + \gamma I_{DD} + I_{AA}}$$

565 Where I_{DA}, I_{AA} and I_{DD} are the background corrected number of photons detected in the
566 acceptor detection channels after donor excitation, in the acceptor detection channels
567 after acceptor excitation and in the donor detection channels after donor excitation,
568 respectively; *α* is a correction factor for the direct excitation of the acceptor with the 483

569 nm laser; δ is a correction factor for the emission crosstalk of the donor in the acceptor
570 channel and *γ* is a correction factor for the relative detection efficiency of the donor and
571 acceptor [34,35].To account for instrument-specific difference of donor and acceptor signal
572 detection efficiencies, the γ correction factor was determined by measuring a mixture of
573 FRET-labeled DNA standards with two different FRET efficiencies and labeled with the
574 same dyes as the LmrP protein (Alexa Fluor 488 and ATTO 647N) . The α and β
575 correction values were determined from the protein measurements itself by fitting . The
576 obtained *E-S* histogram was used to determine the corrections. The reader is referred to
577 Maslov et al. for details on smFRET correction factors[34,59]. The correction values were
578 found to be similar between different measurement repeats. The following correction
579 values were used for the processing of all presented datasets: α = 0.03, δ = 0.03, and γ
580 = 1.2 .

581 **Analysis of Intra-Bursts Dynamics with Hidden-Markov Model Fitting**

582 The processed and blinking-removed set of bursts was used to assess each dataset for
583 the presence of intra-burst dynamics. The processed and cleaned-up list of burst events
584 (see section Burst-wise Data Processing) were loaded into the burstH2MM module
585 (Harris et al., 2022) to quantify and characterize states visited by the FRET-labeled
586 samples. A multiparameter H^2MM fit was carried out (using the $D_{ex}D_{em}$, $D_{ex}A_{em}$, and
587 $A_{ex}A_{em}$ photon streams) with a maximum of 3200 fit iterations to a maximum of five states.
588 The integrated complete likelihood (ICL) criterion was assessed to predict the most likely
589 number of states in the model as described by Harris et al. (2022). The model with the
590 lowest ICL value, or where the states had a mean stoichiometry of S≈0.5, corresponding
591 to FRET active molecules exclusively, was selected for each condition. A model was
592 rejected once the returned mean values for S were markedly different from what can be
593 considered a FRET-active state. This is the case, for example, if an mpH^2MM model has
594 split a state into two states with different *S* compared to the previous model with one state
595 less. We rejected such models with a difference in *S* since no meaningful conformational
596 state can be inferred from such a model. We estimated the mean dwell time for each state
597 from the extracted transition rate constants between states. The mean state dwell time
598 was calculated as tau_i = 1 / ((∑k_i,j) / N_states) as the inverse sum of all exchange rates

599 that depopulate state i divided by the number of depopulation paths. The burst
600 classifications were used to visualize the distribution based on the total burst duration
601 (burst-wise histogram) or per-dwell basis (dwell-based scatter plot). The state-average
602 FRET efficiency was used to compare different conditions. The uncertainty of the
603 transition rates obtained by the best-fitting mpH^{2}MM model was tested with the log-
604 likelihood ratio test which is implemented in the burstH^{2}MM module. The 95%-confidence
605 interval was calculated using the likelihood ratio test, where the log-likelihood was
606 reduced by 1.92 from its optimal value to determine the bounds of the interval.
607 We accounted for the possibility that mpH^{2}MM underfitted the experimental data.
608 However, with a simulated molecule visiting three states, underfitting with a two-state
609 model cannot result in shorter state dwells (see Suppl. Notes). Thus, the observed
610 increase in speed of the conformational change cannot explained by methodological
611 artifacts but rather by an actual acceleration of the conformational landscape of the
612 transporter.
613
614 **Cell survival assay**
615 Mutant and WT LmrP genes were transformed into *L. lactis* strain NZ9000 ΔLmrA
616 ΔLmrCD[42] through electroporation. Individual colonies were grown overnight and used to
617 inoculate 10ml cultures of M17 (supplemented with 0.5% glucose, 5 µg/ml of
618 chloramphenicol), which were then incubated statically at 30 °C until reaching an OD660
619 of ~0.7, when expression was induced through the addition of a 1:1,000 dilution of the
620 supernatant of the nisin-producing *L. lactis* strain NZ900034[52]. After 2 h of expression,
621 cells were diluted with M17 (supplemented with 0.5% glucose, 5 µg/ml of chloramphenicol
622 and 1:1,000 dilution of the supernatant of the nisin-producing L. lactis strain NZ9000) to
623 an OD660 of 0.05. These dilute solutions were then aliquoted into 96-well plates
624 containing a dilution series of antibiotic within the M17 (supplemented with 0.5% glucose,
625 5 µg/ml chloramphenicol and a 1:1,000 dilution of the supernatant of the nisin-producing
626 *L. lactis* strain NZ9000. The plates incubated to at 30 °C, without shaking, for 16 h before
627 measuring the OD660 using Spark Multimode Microplate Reader(Tecan). The assays
628 were conducted for at least three independent times, with six replica for each antibiotic
629 dilution per assay. After OD normalization, the IC50 values and corresponding standard

630 error of the mean data were calculated from a non-linear regression fit (dose–response
631 inhibition model)[62,63] using GraphPad Prism 10.3.

632 Data availability

633 The code used to perform mpH2MM-based analysis of the presented experimental
634 smFRET data is provided on Zenodo :
635 URL: https://zenodo.org/records/19449660
636 DOI: 10.5281/zenodo.19449660
637 (https://doi.org/10.5281/zenodo.19449660)

638 References

639

640 1. Blair, J. M. A., Webber, M. A., Baylay, A. J., Ogbolu, D. O. & Piddock, L. J. V. Molecular
641 mechanisms of antibiotic resistance. *Nat Rev Microbiol* **13**, 42–51 (2015).
642 2. Nikaido, H. Multidrug resistance in bacteria. *Annu Rev Biochem* **78**, 119–146 (2009).
643 3. Du, D. *et al.* Multidrug efflux pumps: structure, function and regulation. *Nat Rev Microbiol*
644 **16**, 523–539 (2018).
645 4. Chitsaz, M. & Brown, M. H. The role played by drug efflux pumps in bacterial multidrug
646 resistance. *Essays Biochem* **61**, 127–139 (2017).
647 5. Mahmood, H. Y., Jamshidi, S., Sutton, J. M. & Rahman, K. M. Current advances in
648 developing inhibitors of bacterial multidrug efflux pumps. *Curr. Med. Chem.* **23**, 1062–1081
649 (2016).
650 6. Colclough, A. L. *et al.* RND efflux pumps in Gram-negative bacteria; regulation, structure
651 and role in antibiotic resistance. *Future Microbiol.* **15**, 143–157 (2020).
652 7. Takatsuka, Y., Chen, C. & Nikaido, H. Mechanism of recognition of compounds of diverse
653 structures by the multidrug efflux pump AcrB of Escherichia coli. *Proc. Natl. Acad. Sci. U. S.*
654 *A.* **107**, 6559–6565 (2010).
655 8. Murakami, S., Nakashima, R., Yamashita, E., Matsumoto, T. & Yamaguchi, A. Crystal

656 structures of a multidrug transporter reveal a functionally rotating mechanism. *Nature* **443**,
657 173–179 (2006).
658 9. Wang, Z. *et al.* An allosteric transport mechanism for the AcrAB-TolC multidrug efflux
659 pump. *Elife* **6**, (2017).
660 10. Du, D. *et al.* Structure of the AcrAB-TolC multidrug efflux pump. *Nature* **509**, 512–515
661 (2014).
662 11. Peterson, E. & Kaur, P. Antibiotic Resistance Mechanisms in Bacteria: Relationships
663 Between Resistance Determinants of Antibiotic Producers, Environmental Bacteria, and
664 Clinical Pathogens. *Front Microbiol* **9**, 2928 (2018).
665 12. Munita, J. M. & Arias, C. A. Mechanisms of Antibiotic Resistance. *Microbiol Spectr* **4**,
666 (2016).
667 13. Ranaweera, I. *et al.* Structural comparison of bacterial multidrug efflux pumps of the major
668 facilitator superfamily. *Trends Cell Mol Biol* **10**, 131–140 (2015).
669 14. Quistgaard, E. M., Löw, C., Guettou, F. & Nordlund, P. Understanding transport by the
670 major facilitator superfamily (MFS): structures pave the way. *Nat Rev Mol Cell Biol* **17**, 123–
671 132 (2016).
672 15. Jardetzky, O. Simple allosteric model for membrane pumps. *Nature* **211**, 969–970 (1966).
673 16. Bolhuis, H. *et al.* The Lactococcal lmrP gene encodes a proton motive force-dependent
674 drug transporter. *J. Biol. Chem.* **270**, 26092–26098 (1995).
675 17. Roth, A. & Govaerts, C. LmrP from Lactoccoccus lactis: a tractable model to understand
676 secondary multidrug transport in MFS. *Res Microbiol* **169**, 468–477 (2018).
677 18. Putman, M., van Veen, H. W., Degener, J. E. & Konings, W. N. The lactococcal secondary
678 multidrug transporter LmrP confers resistance to lincosamides, macrolides, streptogramins
679 and tetracyclines. *Microbiology* **147**, 2873–2880 (2001).
680 19. Masureel, M. *et al.* Protonation drives the conformational switch in the multidrug transporter
681 LmrP. *Nat. Chem. Biol.* **10**, 149–155 (2014).

682 20. Martens, C. *et al.* Lipids modulate the conformational dynamics of a secondary multidrug
683 transporter. *Nat. Struct. Mol. Biol.* **23**, 744–751 (2016).
684 21. Claxton, D. P., Kazmier, K., Mishra, S. & Mchaourab, H. S. Navigating membrane protein
685 structure, dynamics, and energy landscapes using spin labeling and EPR spectroscopy.
686 *Methods Enzymol.* **564**, 349–387 (2015).
687 22. Pao, S. S., Paulsen, I. T. & Saier, M. H., Jr. Major facilitator superfamily. *Microbiol. Mol.*
688 *Biol. Rev.* **62**, 1–34 (1998).
689 23. Drew, D., North, R. A., Nagarathinam, K. & Tanabe, M. Structures and general transport
690 mechanisms by the major facilitator superfamily (MFS). *Chem. Rev.* **121**, 5289–5335
691 (2021).
692 24. Debruycker, V. *et al.* An embedded lipid in the multidrug transporter LmrP suggests a
693 mechanism for polyspecificity. *Nat Struct Mol Biol* **27**, 829–835 (2020).
694 25. Levring, J. *et al.* CFTR function, pathology and pharmacology at single-molecule resolution.
695 *Nature* **616**, 606–614 (2023).
696 26. Huysmans, G. H. M., Ciftci, D., Wang, X., Blanchard, S. C. & Boudker, O. The high-energy
697 transition state of the glutamate transporter homologue GltPh. *EMBO J.* **40**, e105415
698 (2021).
699 27. Akyuz, N. *et al.* Transport domain unlocking sets the uptake rate of an aspartate
700 transporter. *Nature* **518**, 68–73 (2015).
701 28. Husada, F. *et al.* Conformational dynamics of the ABC transporter McjD seen by single-
702 molecule FRET. *EMBO J* **37**, (2018).
703 29. Mazal, H. & Haran, G. Single-molecule FRET methods to study the dynamics of proteins at
704 work. *Curr. Opin. Biomed. Eng.* **12**, 8–17 (2019).
705 30. Schuler, B. & Hofmann, H. Single-molecule spectroscopy of protein folding dynamics--
706 expanding scope and timescales. *Curr. Opin. Struct. Biol.* **23**, 36–47 (2013).
707 31. Agam, G. *et al.* Reliability and accuracy of single-molecule FRET studies for

708 characterization of structural dynamics and distances in proteins. *Nat. Methods* **20**, 523–
709 535 (2023).
710 32. Bartels, K., Lasitza-Male, T., Hofmann, H. & Löw, C. Single-Molecule FRET of Membrane
711 Transport Proteins. *Chembiochem* **22**, 2657–2671 (2021).
712 33. Sasmal, D. K., Pulido, L. E., Kasal, S. & Huang, J. Single-molecule fluorescence resonance
713 energy transfer in molecular biology. *Nanoscale* **8**, 19928–19944 (2016).
714 34. Maslov, I. *et al.* Sub-millisecond conformational dynamics of the A adenosine receptor
715 revealed by single-molecule FRET. *Commun Biol* **6**, 362 (2023).
716 35. Kudryavtsev, V. *et al.* Combining MFD and PIE for accurate single-pair Förster resonance
717 energy transfer measurements. *Chemphyschem* **13**, 1060–1078 (2012).
718 36. Del Alamo, D., Govaerts, C. & Mchaourab, H. S. AlphaFold2 predicts the inward-facing
719 conformation of the multidrug transporter LmrP. *Proteins* **89**, 1226–1228 (2021).
720 37. Santoso, Y., Torella, J. P. & Kapanidis, A. N. Characterizing single-molecule FRET
721 dynamics with probability distribution analysis. *Chemphyschem* **11**, 2209–2219 (2010).
722 38. Tsukanov, R., Tomov, T. E., Berger, Y., Liber, M. & Nir, E. Conformational dynamics of
723 DNA hairpins at millisecond resolution obtained from analysis of single-molecule FRET
724 histograms. *J. Phys. Chem. B* **117**, 16105–16109 (2013).
725 39. Harris, P. D. *et al.* Multi-parameter photon-by-photon hidden Markov modeling. *Nat*
726 *Commun* **13**, 1000 (2022).
727 40. Pirchi, M. *et al.* Photon-by-Photon Hidden Markov Model Analysis for Microsecond Single-
728 Molecule FRET Kinetics. *J Phys Chem B* **120**, 13065–13075 (2016).
729 41. Putman, M., van Veen, H. W. & Konings, W. N. Molecular properties of bacterial multidrug
730 transporters. *Microbiol. Mol. Biol. Rev.* **64**, 672–693 (2000).
731 42. Venter, H., Velamakanni, S., Balakrishnan, L. & van Veen, H. W. On the energy-
732 dependence of Hoechst 33342 transport by the ABC transporter LmrA. *Biochem.*
733 *Pharmacol.* **75**, 866–874 (2008).

734 43. Brawley, D. N. *et al.* Structural basis for inhibition of the drug efflux pump NorA from
735 Staphylococcus aureus. *Nat. Chem. Biol.* **18**, 706–712 (2022).
736 44. Kowalska-Krochmal, B. & Dudek-Wicher, R. The minimum inhibitory concentration of
737 antibiotics: Methods, interpretation, clinical relevance. *Pathogens* **10**, 165 (2021).
738 45. Majumder, P. *et al.* Cryo-EM structure of antibacterial efflux transporter QacA from
739 Staphylococcus aureus reveals a novel extracellular loop with allosteric role. *EMBO J.* **42**,
740 e113418 (2023).
741 46. Li, J. *et al.* Proton-coupled transport mechanism of the efflux pump NorA. *Nat. Commun.*
742 **15**, 4494 (2024).
743 47. Edgar, R. & Bibi, E. MdfA, an Escherichia coli multidrug resistance protein with an
744 extraordinarily broad spectrum of drug recognition. *J. Bacteriol.* **179**, 2274–2280 (1997).
745 48. Bolhuis, H. *et al.* Energetics and mechanism of drug transport mediated by the lactococcal
746 multidrug transporter LmrP. *J. Biol. Chem.* **271**, 24123–24128 (1996).
747 49. Yardeni, E. H., Mishra, S., Stein, R. A., Bibi, E. & Mchaourab, H. S. The multidrug
748 transporter MdfA deviates from the canonical model of alternating access of MFS
749 transporters. *J. Mol. Biol.* **432**, 5665–5680 (2020).
750 50. Heng, J. *et al.* Substrate-bound structure of the E. coli multidrug resistance transporter
751 MdfA. *Cell Res.* **25**, 1060–1073 (2015).
752 51. Putman, M., van Veen, H. W., Poolman, B. & Konings, W. N. Restrictive use of detergents
753 in the functional reconstitution of the secondary multidrug transporter LmrP. *Biochemistry*
754 **38**, 1002–1008 (1999).
755 52. Kuipers, O. P., Beerthuyzen, M. M., Siezen, R. J. & De Vos, W. M. Characterization of the
756 nisin gene cluster nisABTCIPR of Lactococcus lactis. Requirement of expression of the
757 nisA and nisI genes for development of immunity. *Eur. J. Biochem.* **216**, 281–291 (1993).
758 53. Mierau, I. & Kleerebezem, M. 10 years of the nisin-controlled gene expression system
759 (NICE) in Lactococcus lactis. *Appl. Microbiol. Biotechnol.* **68**, 705–717 (2005).

760 54. Kalinin, S. *et al.* A toolkit and benchmark study for FRET-restrained high-precision
761 structural modeling. *Nature Methods* **9**, 1218–1225 (2012).
762 55. Vandenberk, N., Barth, A., Borrenberghs, D., Hofkens, J. & Hendrix, J. Evaluation of Blue
763 and Far-Red Dye Pairs in Single-Molecule Förster Resonance Energy Transfer
764 Experiments. *The Journal of Physical Chemistry B* (2018) doi:10.1021/acs.jpcb.8b00108.
765 56. Monk, I. R., Casey, P. G., Hill, C. & Gahan, C. G. M. Directed evolution and targeted
766 mutagenesis to murinize Listeria monocytogenes internalin A for enhanced infectivity in the
767 murine oral infection model. *BMC Microbiol* **10**, 318 (2010).
768 57. Liu, H. & Naismith, J. H. An efficient one-step site-directed deletion, insertion, single and
769 multiple-site plasmid mutagenesis protocol. *BMC Biotechnology* **8**, 1–10 (2008).
770 58. Hendrix, J. & Lamb, D. C. Pulsed interleaved excitation: principles and applications.
771 *Methods Enzymol.* **518**, 205–243 (2013).
772 59. Tomov, T. E. *et al.* Disentangling subpopulations in single-molecule FRET and ALEX
773 experiments with photon distribution analysis. *Biophys. J.* **102**, 1163–1173 (2012).
774 60. Ingargiola, A., Lerner, E., Chung, S., Weiss, S. & Michalet, X. FRETBursts: An Open
775 Source Toolkit for Analysis of Freely-Diffusing Single-Molecule FRET. *PLoS One* **11**,
776 e0160716 (2016).
777 61. Kache, T. & Hendrix, J. H^{2}MM-guided removal of dye blinking effects from single-
778 molecule FRET burst data. *BMC Methods* **2**, (2025).
779 62. Lyles, R. H., Poindexter, C., Evans, A., Brown, M. & Cooper, C. R. Nonlinear model-based
780 estimates of IC(50) for studies involving continuous therapeutic dose-response data.
781 *Contemp. Clin. Trials* **29**, 878–886 (2008).
782 63. Sebaugh, J. L. Guidelines for accurate EC50/IC50 estimation. *Pharm. Stat.* **10**, 128–134
783 (2011).
784
785

Acknowledgements

This work was supported by the FNRS (MIS grant number F45322.22 and CDR J0142 24F) , by an ARC Consolidator grant from the ULB (grant number 4110F000129), and the Jaumotte Demoulin Foundation for C.M. A. R. was a Research Fellow of the F.R.I.A. H.M is funded by a scientific collaborator fellowship “collaborateur scientifique” by The National Fund for Scientific Research (Le Fonds de la Recherche Scientifique – FNRS) with grant number FC 59497. T. K. was funded by a PhD fellowship from Flemish Research Foundation (*Fonds Wetenschappelijk Onderzoek*, FWO) with grant number 11N4722N. C.G. is a Senior Research Associate of the F.R.S.-F.N.R.S.

Author Contributions

C.G, C.M and J.H conceived the study. H.M and T.K designed the experiments. A.R performed the mutagenesis, H.M, A.R and T.K carried out the smFRET experiments and analyzed the data. C.M and H.M wrote the paper with input from all authors.

Competing Financial Interests Statement

The authors declare no competing financial interests.

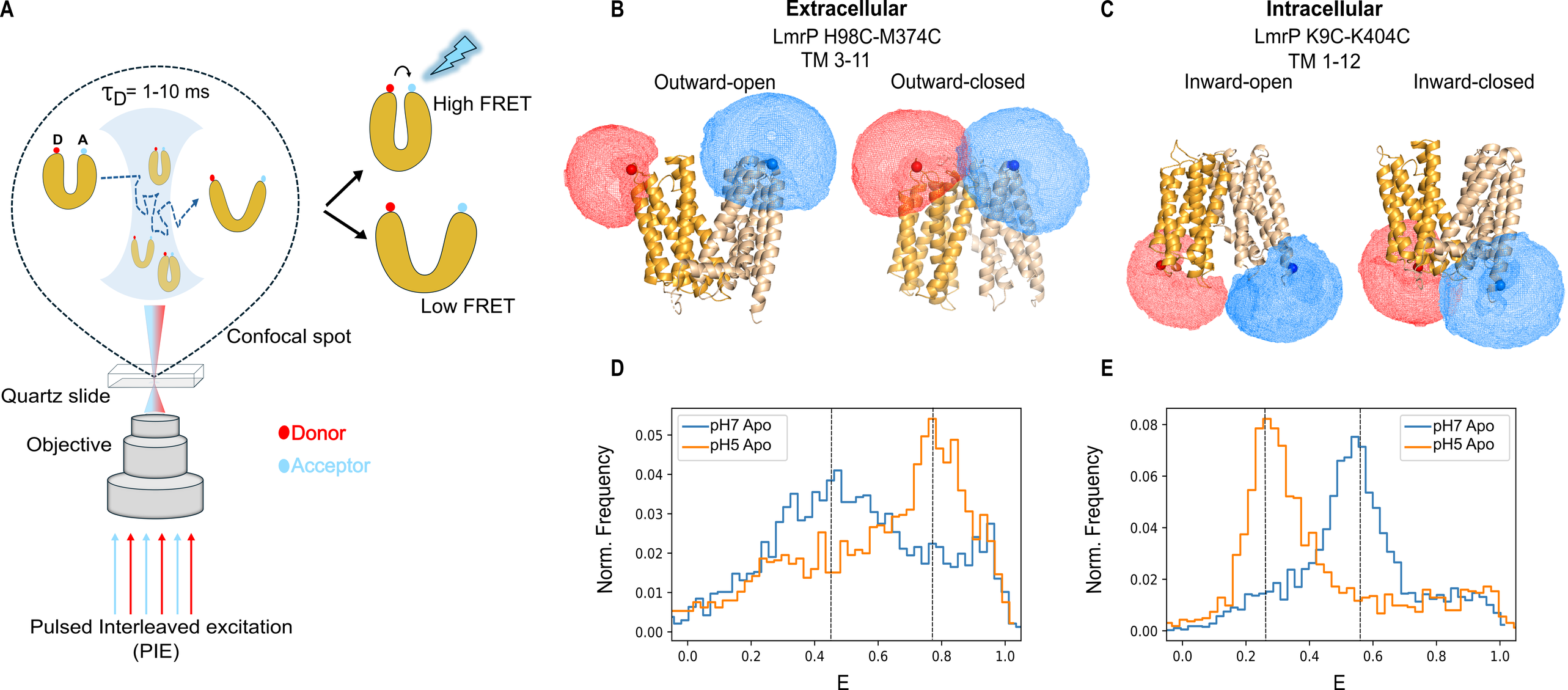
A
τD= 1-10 ms
D
A
High FRET
Low FRET
Confocal spot
Quartz slide
Objective
Donor
Acceptor
Pulsed Interleaved excitation
(PIE)
B
Extracellular
LmrP H98C-M374C
TM 3-11
Outward-open
Outward-closed
C
Intracellular
LmrP K9C-K404C
TM 1-12
Inward-open
Inward-closed
D
pH7 Apo
pH5 Apo
Norm. Frequency
E
E
pH7 Apo
pH5 Apo
Norm. Frequency
E

A

pH 7

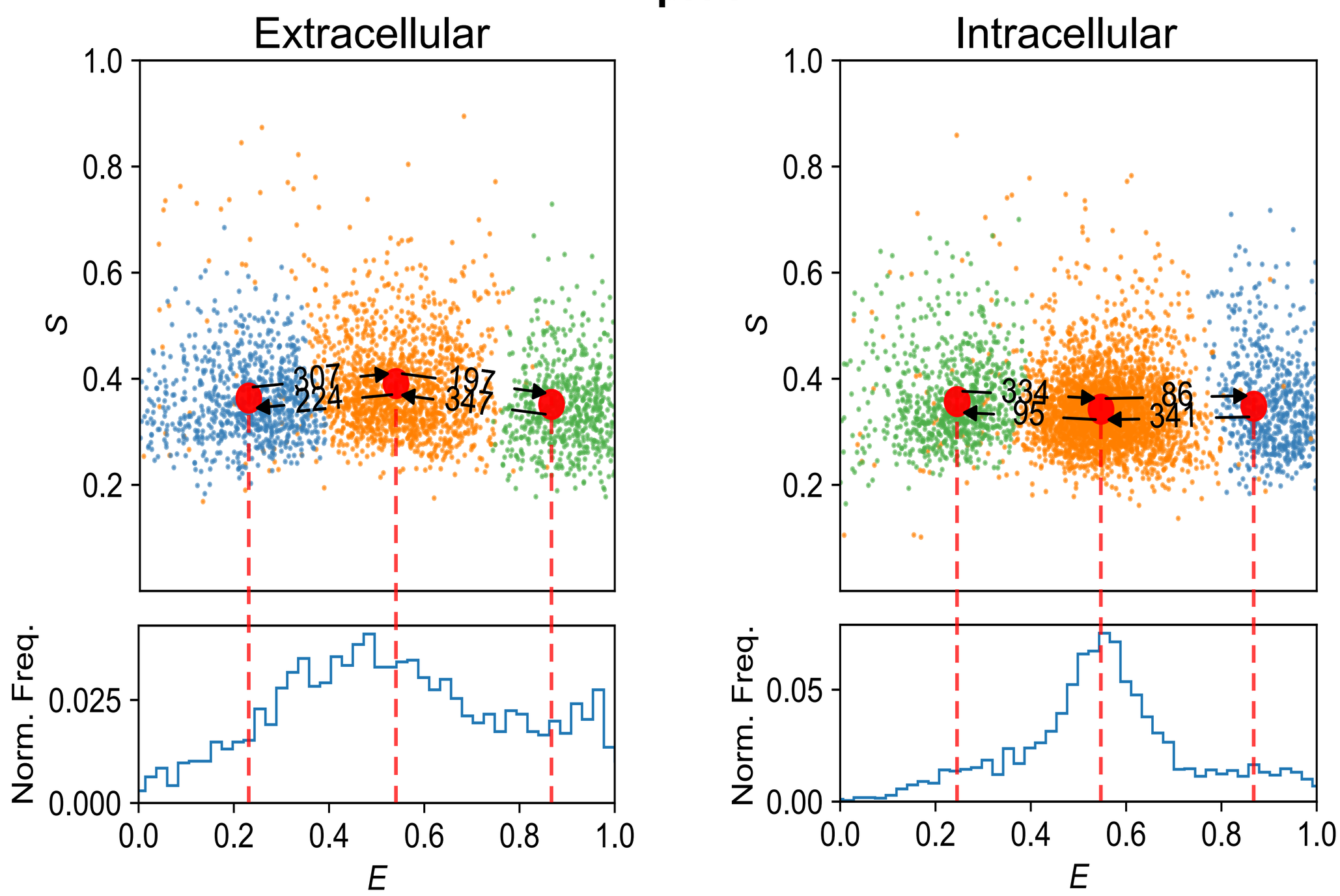

	L_E ⇋	M_E ⇌	H_E	L_I ⇋	M_I ⇌	H_I
E	0.22	0.54	0.86	0.24	0.54	0.86
Mean dwell time	3.2ms	4.7ms	2.9ms	2.9ms	11ms	2.9ms

B

pH 5

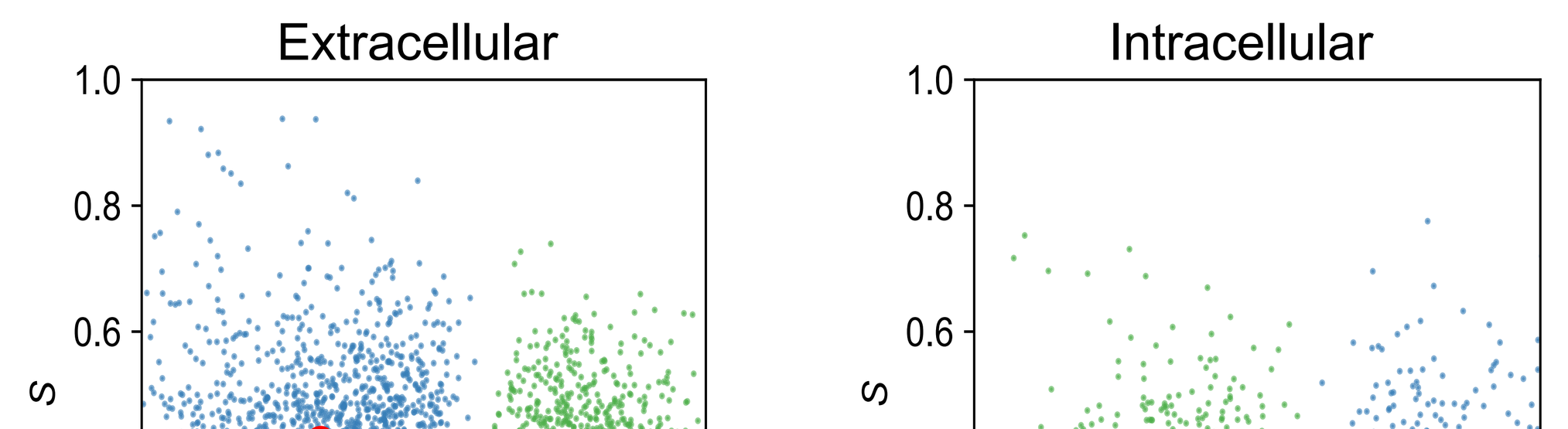

	L_E ⇋	H_E	L_I ⇌	H_I
E	0.31	0.78	0.31	0.82
Mean dwell time	3.2ms	4.7ms	14.7ms	4.1ms

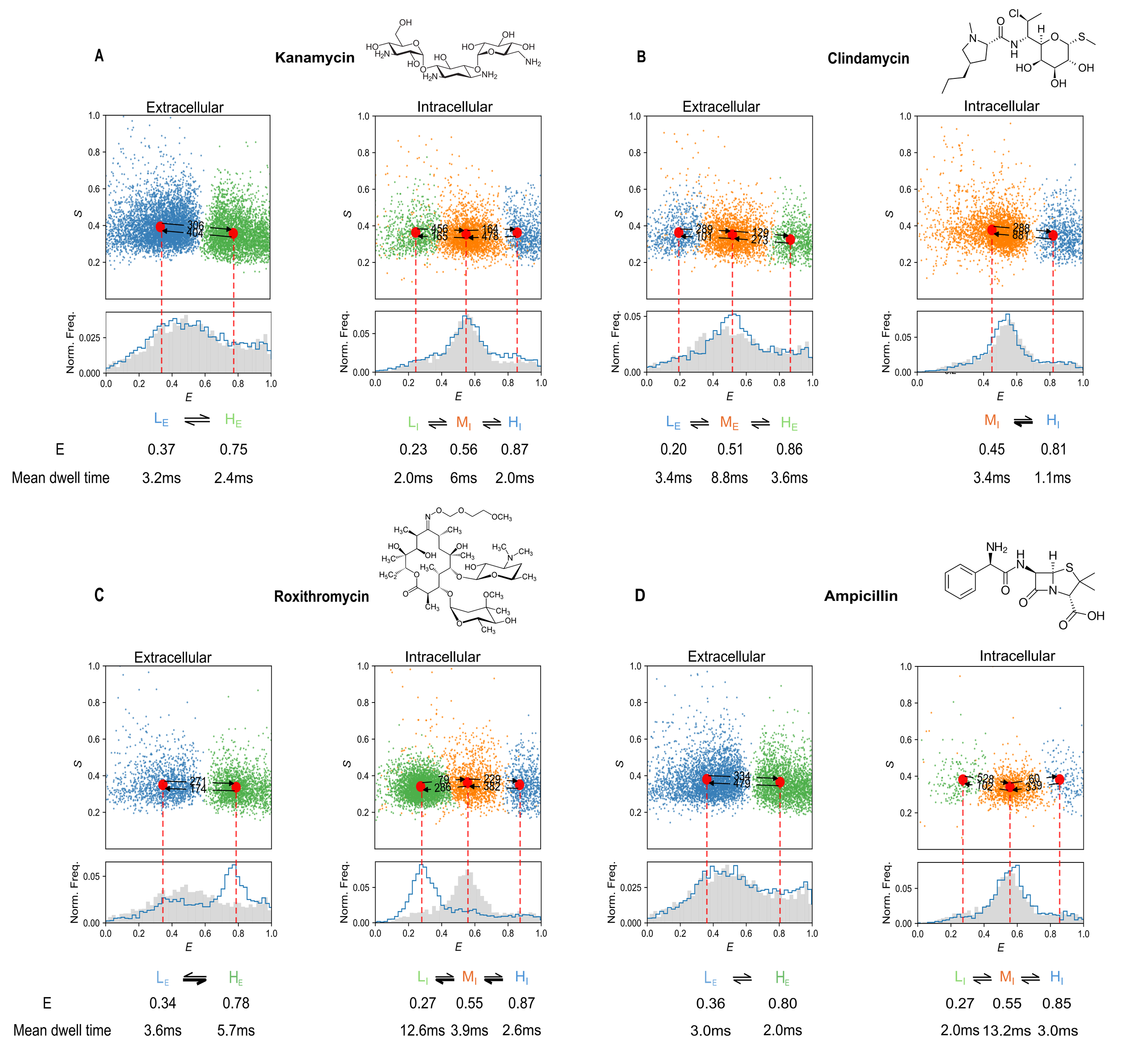
A
Kanamycin
Extracellular
Intracellular
B
Clindamycin
Extracellular
Intracellular
C
Roxithromycin
Extracellular
Intracellular
D
Ampicillin
Extracellular
Intracellular
S
E
Norm. Freq.
306
404
456
165
164
478
289
101
129
273
288
881
271
174
79
286
229
382
394
479
528
102
60
339
$L_E \rightleftharpoons H_E$
$L_I \rightleftharpoons M_I \rightleftharpoons H_I$
$L_E \rightleftharpoons M_E \rightleftharpoons H_E$
$M_I \rightleftharpoons H_I$
$L_E \rightleftharpoons H_E$
$L_I \rightleftharpoons M_I \rightleftharpoons H_I$
$L_E \rightleftharpoons H_E$
$L_I \rightleftharpoons M_I \rightleftharpoons H_I$
E 0.37 0.75
Mean dwell time 3.2ms 2.4ms
0.23 0.56 0.87
2.0ms 6ms 2.0ms
0.20 0.51 0.86
3.4ms 8.8ms 3.6ms
0.45 0.81
3.4ms 1.1ms
E 0.34 0.78
Mean dwell time 3.6ms 5.7ms
0.27 0.55 0.87
12.6ms 3.9ms 2.6ms
0.36 0.80
3.0ms 2.0ms
0.27 0.55 0.85
2.0ms 13.2ms 3.0ms

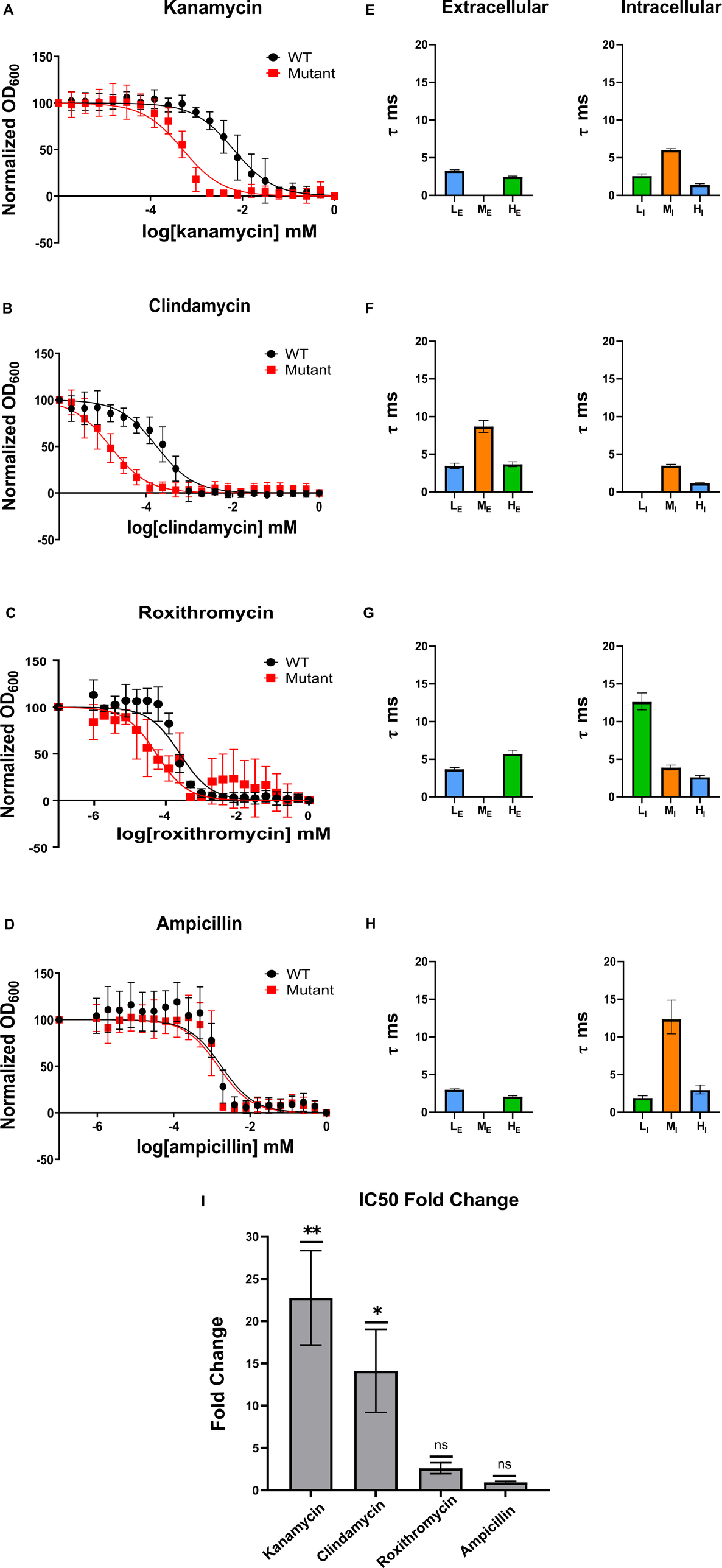
A
Kanamycin
WT
Mutant
Normalized OD600
log[kanamycin] mM
B
Clindamycin
log[clindamycin] mM
C
Roxithromycin
log[roxithromycin] mM
D
Ampicillin
log[ampicillin] mM
E
Extracellular
Intracellular
F
G
H
τ ms
LE
ME
HE
LI
MI
HI
I
IC50 Fold Change
Fold Change
**
*
ns
ns
Kanamycin
Clindamycin
Roxithromycin
Ampicillin

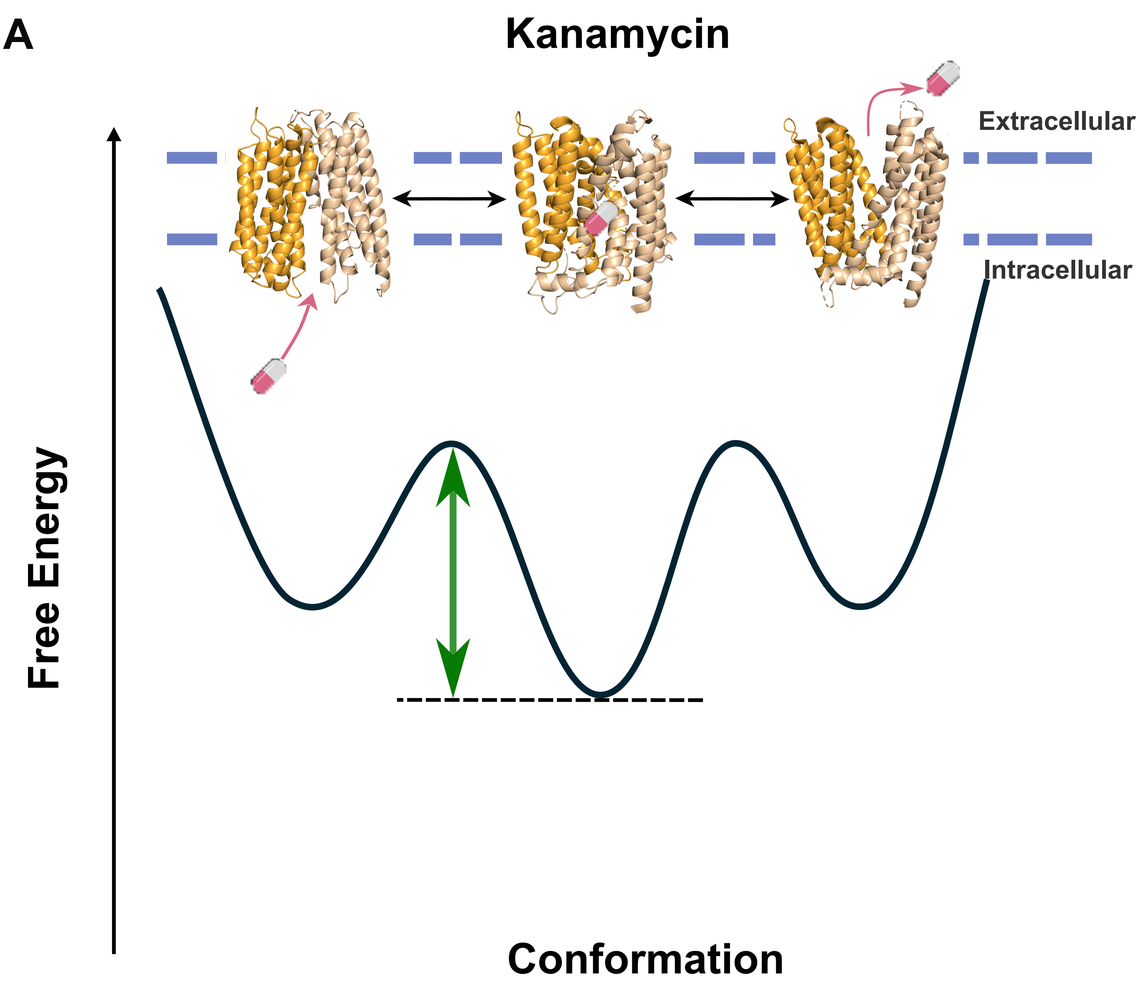
A
Kanamycin
Extracellular
Intracellular
Free Energy
Conformation

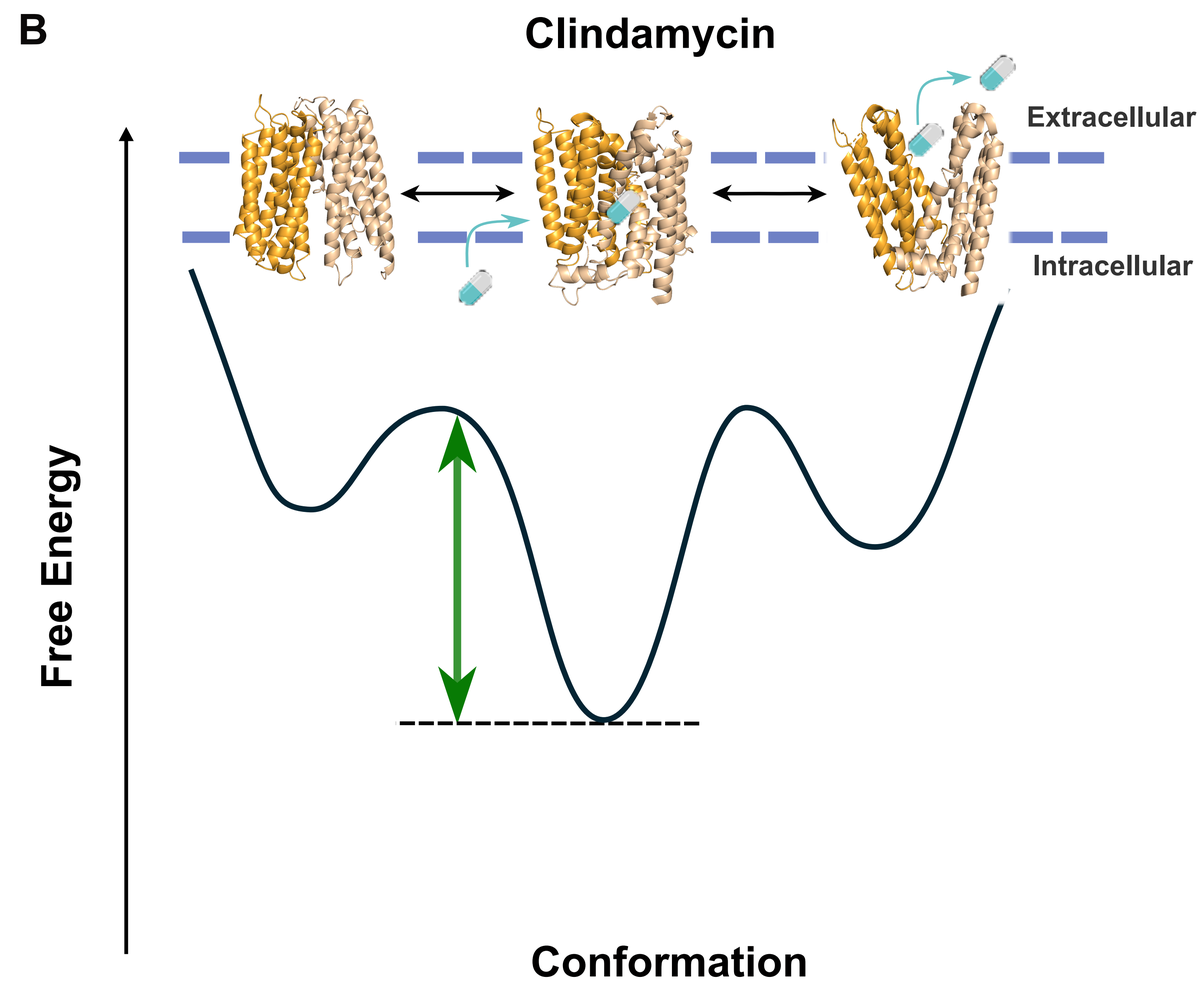
B
Clindamycin
Extracellular
Intracellular
Free Energy
Conformation

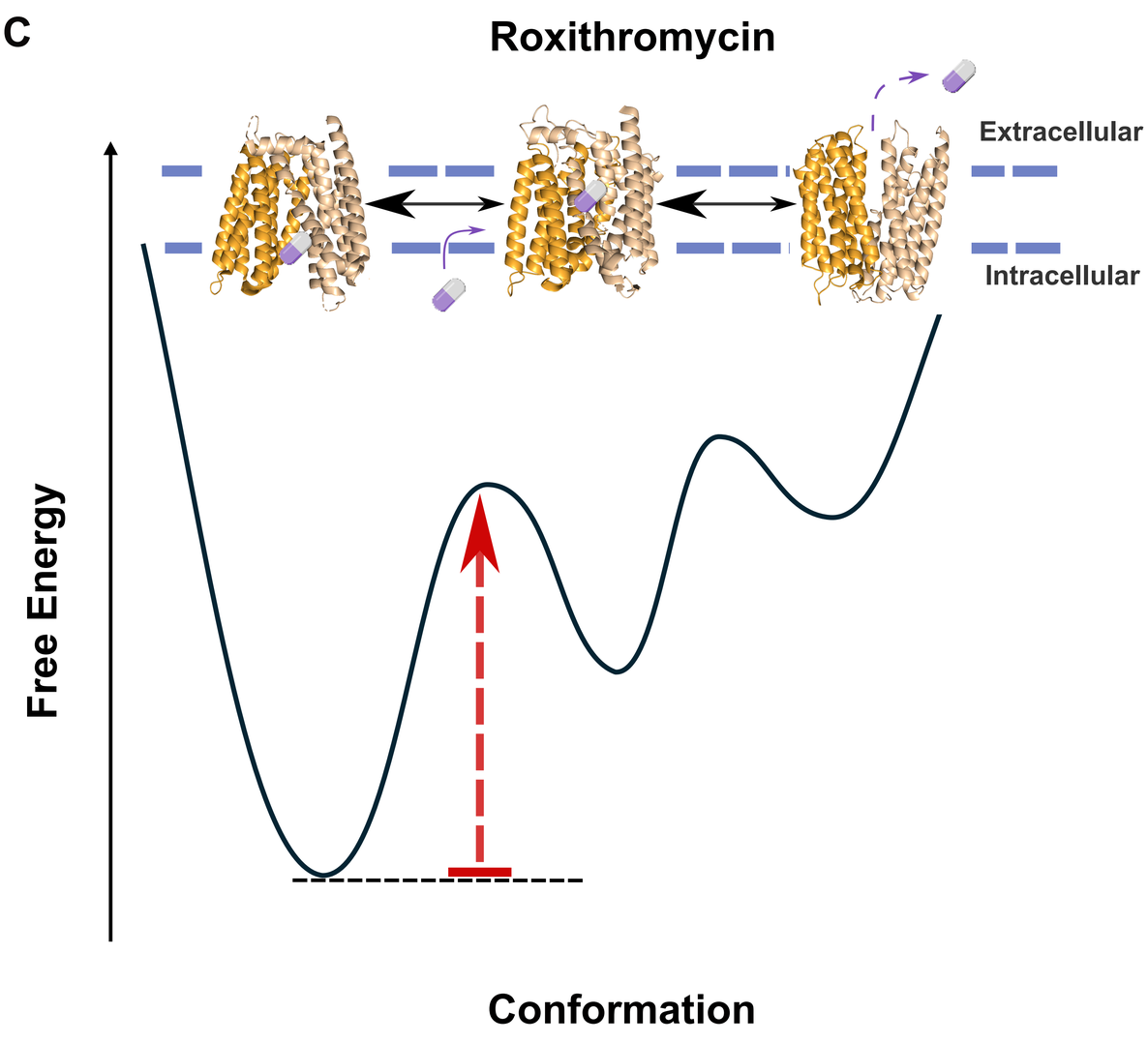
C
Roxithromycin
Extracellular
Intracellular
Free Energy
Conformation

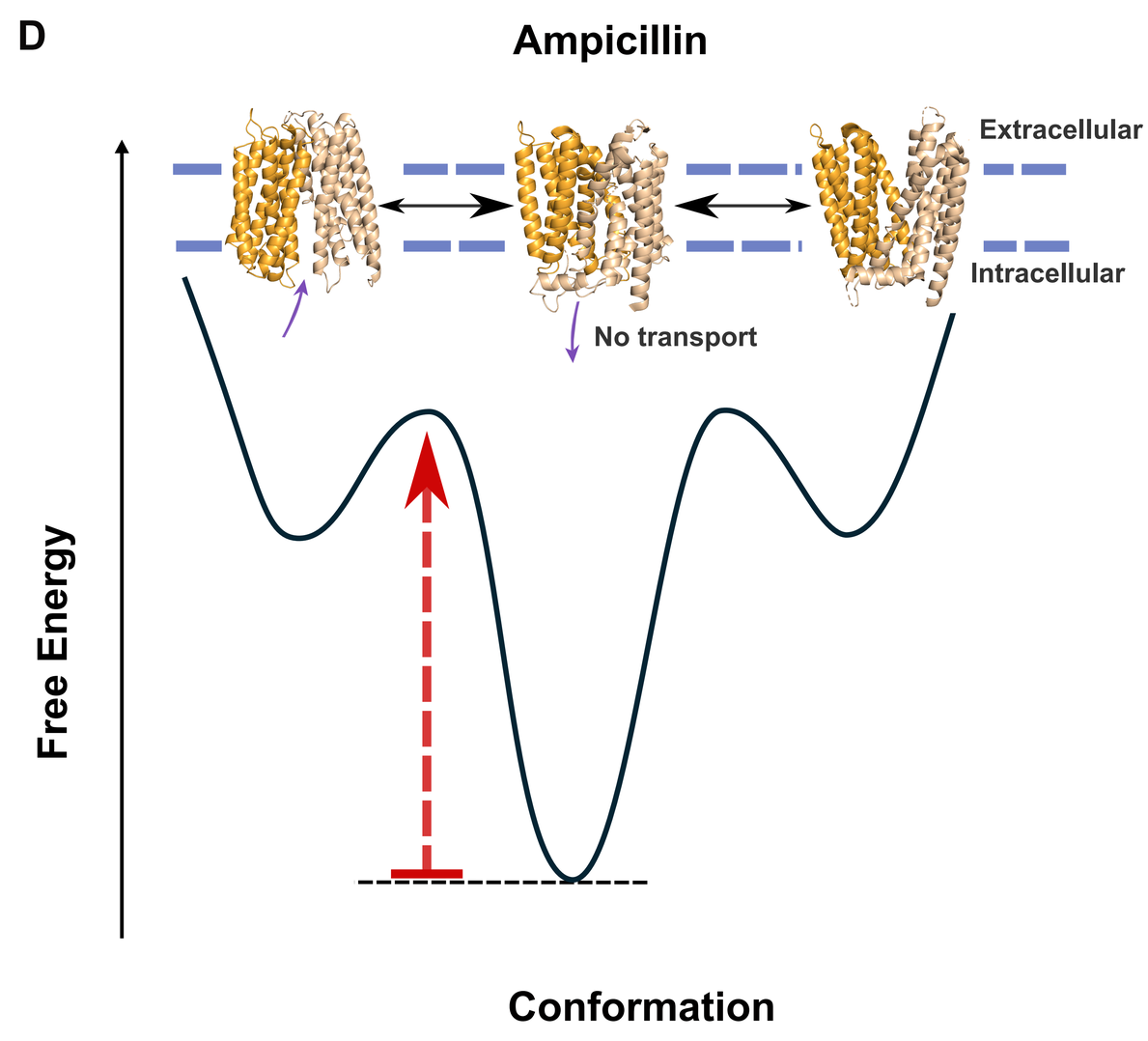
D
Ampicillin
Extracellular
Intracellular
No transport
Free Energy
Conformation